



Characterization of Geochemistry in Hydrothermal Sediments From the Newly Discovered Onnuri Vent Field in the Middle Region of the Central Indian Ridge

Dhongil Lim^{1,2*}, Jihun Kim^{1,2}, Wonnyon Kim¹, Jonguk Kim¹, Dongsung Kim¹, Le Zhang³, Kyungun Kwack¹ and Zhaokai Xu^{4,5,6*}

¹ Korea Institute of Ocean Science & Technology, Busan, South Korea, ² Department of Ocean Science, KIOST School, University of Science & Technology, Daejeon, South Korea, ³ State Key Laboratory of Isotope Geochemistry, Guangzhou Institute of Geochemistry, Chinese Academy of Sciences, Guangzhou, China, ⁴ CAS Key Laboratory of Marine Geology and Environment, Institute of Oceanology, Chinese Academy of Sciences, Qingdao, China, ⁵ Center for Ocean Mega-Science, Chinese Academy of Sciences, Qingdao, China, ⁶ CAS Center for Excellence in Quaternary Science and Global Change, Xi'an, China

OPEN ACCESS

Edited by:

Pei-Yuan Qian,
Hong Kong University of Science
and Technology, Hong Kong SAR,
China

Reviewed by:

Rebecca Zitoun,
Royal Netherlands Institute for Sea
Research (NIOZ), Netherlands
Pavlos Megalovasilis,
University of Patras, Greece

*Correspondence:

Dhongil Lim
oceanlim@kiost.ac.kr
Zhaokai Xu
zhaokaixu@qdio.ac.cn

Specialty section:

This article was submitted to
Deep-Sea Environments and Ecology,
a section of the journal
Frontiers in Marine Science

Received: 08 November 2021

Accepted: 11 January 2022

Published: 11 February 2022

Citation:

Lim D, Kim J, Kim W, Kim J,
Kim D, Zhang L, Kwack K and Xu Z
(2022) Characterization
of Geochemistry in Hydrothermal
Sediments From the Newly
Discovered Onnuri Vent Field
in the Middle Region of the Central
Indian Ridge.
Front. Mar. Sci. 9:810949.
doi: 10.3389/fmars.2022.810949

The recently discovered Onnuri hydrothermal vent field (OVF) is a typical off-axis ultramafic-hosted vent system, located on the summit of the dome-like ocean core complex (OCC) at a distance of ~12 km from the ridge axis along the middle region of the Central Indian Ridge (CIR). The plume chemistry with high methane anomaly was consistent with the precursor of hydrothermal activity; however, the fundamental characteristic of the OVF system, such as the hydrothermal circulation process and source of heat, remains poorly understood. Here, we focus on the geochemical features of surface sediments and minerals collected at and around the OVF region in order to better understand this venting system. The results reveal that the OVF sediments are typified by remarkably high concentrations of Fe, Si, Ba, Cu, and Zn, derived from hydrothermal fluid and S and Mg from seawater; depleted C-S isotope compositions; and abundant hydrothermally precipitated minerals (i.e., Fe–Mn hydroxides, sulfide and sulfate minerals, and opal silica). Notably, the occurrence of pure talc and barite bears witness to strong hydrothermal activity in the OVF, and their sulfur and strontium isotope geochemistry agree with extensive mixing of the unmodified seawater with high-temperature fluid derived from the gabbroic rock within the ultramafic-dominated ridge segment. The findings reveal that the OVF is a representative example of an off-axis, high-temperature hydrothermal circulation system, possibly driven by the exothermic serpentinization of exposed peridotites. Given the widespread distribution of OCC with detachment faults, furthermore, the OVF may be the most common type of hydrothermal activity in the CIR, although the paucity of data precludes generalizing this result. This study provides important information contributing to our understanding of the ultramafic-hosted hydrothermal vent system with a non-magmatic heat source along mid-ocean ridges.

Keywords: hydrothermal sediments, talc and barite, geochemistry, serpentinization, Central Indian ridges

INTRODUCTION

Because of the importance of the hydrothermal vent system in ocean chemistry, earth dynamics, and biological communities, as well as the increasing interest in massive metal deposits, the exploration of mid-ocean ridges has recently increased dramatically, revealing considerable diversity in hydrothermal systems. Hundreds of hydrothermal vents (more than 500 sites), including hydrothermal sulfide deposits, have been discovered and investigated, mainly in the Pacific and Atlantic Oceans (Hannington et al., 2011; Beaulieu et al., 2013, 2015; German and Seyfried, 2014). In the Indian Ocean ridges that are up to approximately 18,000 km in length (28% of the global total), however, only a few hydrothermal vent sites (i.e., the Dodo, Solitaire, Edmond, Kairei, and Longqi vent fields) have been visually confirmed (e.g., Nakamura et al., 2012 and reference therein; Tao et al., 2012). In the Indian Ocean ridges with various spreading rates (<12–60 mm/yr in full spreading rate), the hydrothermal vent systems are expected to vary in accordance with diverse geological and tectonic features (German et al., 1998; Wang et al., 2011; Beaulieu et al., 2015); however, these ridges remain underexplored relative to the Pacific and Atlantic ridges, and thus available data regarding their hydrothermal vents is still very limited. In this respect, recent systematic ridge expeditions at the Central and Southwest Indian regions and their results have been receiving scientific attention (e.g., Son et al., 2014; Park et al., 2017; Suo et al., 2017; Liao et al., 2018a,b, 2019; Zhou et al., 2018; Choi et al., 2021).

Systematic deep-sea exploration recently uncovered four new active hydrothermal vent fields in the middle region of the Central Indian Ridge (CIR) between 8 and 14°S, where ridge morphology and tectonic structure (e.g., detachment faults and ocean core complexes, OCCs) control increased plume incidence at ridge flank and rift wall locations (Kim et al., 2020). These hydrothermal vent fields, located more than 800 km north of previously known vent fields (i.e., the Dodo and Solitaire fields, Nakamura and Takai, 2015) are characterized by particle-poor, diffuse venting with abundant vent fauna and sulfide deposition. Notably, these new hydrothermal vents show diverse venting styles and plume compositions, attributed to distinctive hydrothermal fluid formation conditions and transport pathways in the slow- to ultraslow-rate spreading ridge setting (Son et al., 2014; Kim et al., 2020). In particular, the Onnuri hydrothermal vent field (OVF) site, located on the summit of OCC at a water depth of ~2,000 m in Segment 3 (Figures 1A–C), is attracting considerable scientific attention because of its isolated location, diffuse venting style, methane-rich plume composition, ultramafic-hosted system, and community of hydrothermal vent fauna. Specifically, water column plumes from this vent site are characterized by negative oxidation-reduction potential anomalies, high dissolved methane (CH₄) concentrations, and low dissolved metal concentrations (Kim et al., 2020). Interestingly, the preliminary observation and plume chemistry suggest that the OVF may be a low-temperature hydrothermal vent, probably supported by the exothermic serpentinization process (Kim et al., 2020). This venting system is thus quite different from the well-known basaltic-hosted venting

systems of high-temperature and metal-rich black smoker, driven by magmatic activity in the CIR (e.g., Dodo and Edmond sites, Tivey, 2007; Nakamura and Takai, 2015). However, solid evidence for the serpentinization reaction (e.g., heat source) and the fluid temperature of the OVF is still lacking.

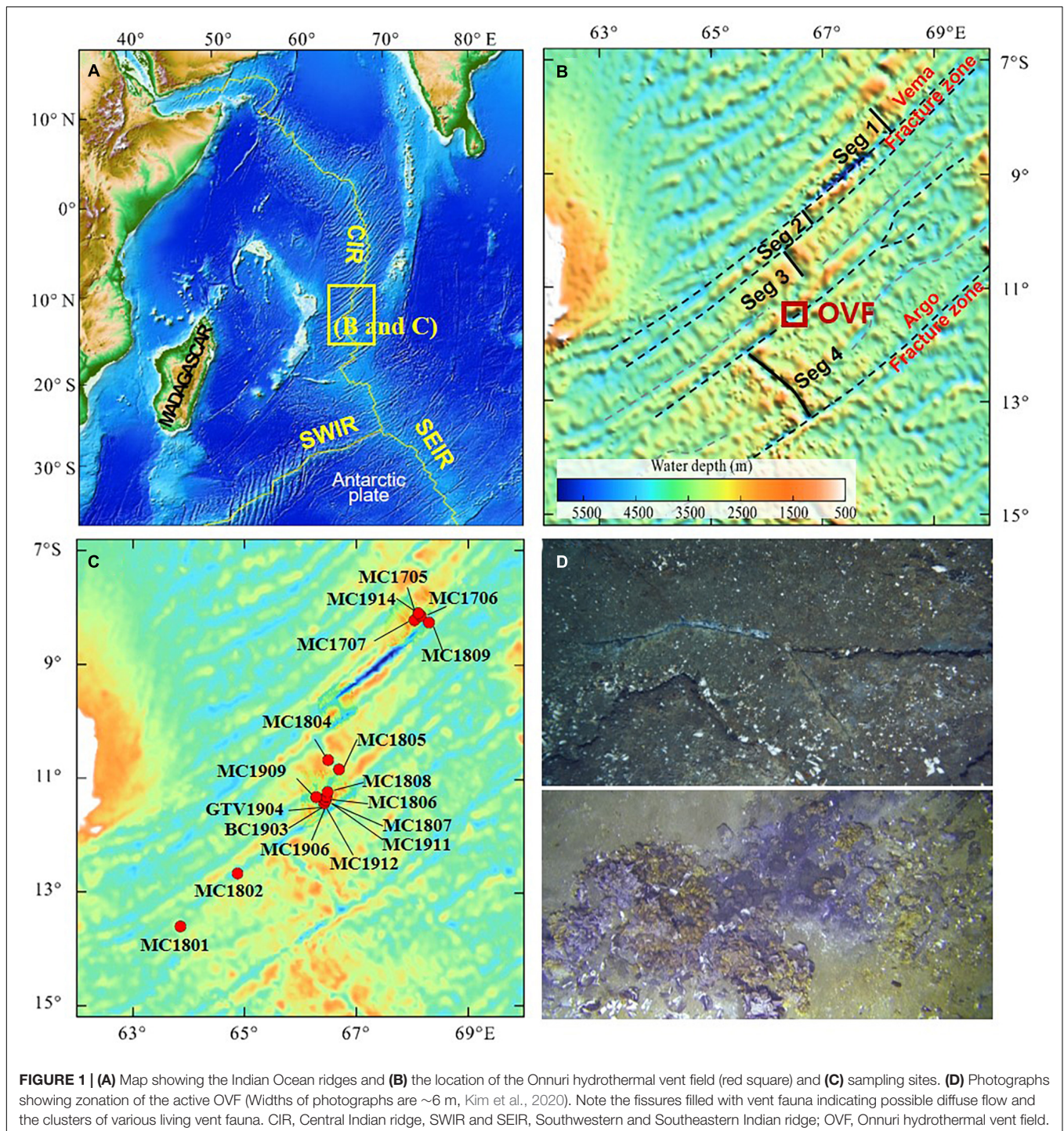
Recently, hydrothermal sediments and minerals have received increasing attention because their geochemical signatures can provide useful information for grasping the character of the associated hydrothermal system, such as the composition, source, and temperature of the fluid, the source of heat, and the process of seawater/fluid interaction (e.g., Cave et al., 2002; D'Orazio et al., 2004; Dias and Barriga, 2006; Dekov et al., 2011; Eickmann et al., 2014; Liao et al., 2019; Zhang et al., 2020). In particular, sulfur and strontium isotopic compositions of hydrothermal minerals – barite and talc – strongly depend on the fluid from which they precipitate and are therefore ideal for tracing the nature of fluid/rock interaction and estimating the formation temperatures of the minerals (e.g., Paytan et al., 1993; Melekestseva et al., 2014; Zhang et al., 2020). In the ultramafic-hosted OVF with a low magma supply, the hydrothermal process and fluid composition are expected to result in different geochemical compositions of sediments compared to those of magma-driven, basalt-hosted hydrothermal vent fields. However, geochemical and mineralogical investigations of the ultramafic-hosted vent sediments are relatively poor.

In this study, we present geochemical (elemental and isotopic compositions) and mineralogical features of hydrothermal sediments (conceivably containing distinct hydrothermal components), collected in and around the OVF in the middle region of the CIR. Of particular interest in this study is the occurrence of peculiar hydrothermal minerals (i.e., hydrothermal talc and barite) and their geochemical and isotopic compositions, providing deeper insights into nature of this hydrothermal vent system. The implications of this study, including new geochemical-mineralogical data regarding the hydrothermal deposits in the CIR, include the ability of the OVF to contribute valuable information for better understanding of hydrothermal vent systems in the Indian Ocean.

STUDY AREA

The middle region of CIR (8–18°S; approximately 700 km of ridge length) is typical of slow-spreading ridges (34–45 mm/yr in full spreading rate, Park et al., 2017), with axial valleys of 500–1000 m relief and spreading segments connected by transform faults and non-transform offsets (Son et al., 2014). OCCs exposed by detachment faults are common features in this area and may lead to extensive hydrothermal circulation at off-axis sites; notably, these faults may be the primary path for hydrothermal fluids that ascend in off-axis regions (Boschi et al., 2008; Park et al., 2017). The OVF with abundant vent fauna located on the summit of dome-like OCC (11°24.9'S, 66°25.4'E; a water depth of ~2,000 m) at a distance of approximately 12 km from the axial neo-volcanic zone.

The OVF's general characteristics (e.g., bathymetry, geological settings, basement rock compositions, plume chemistry, and



fauna diversity) were outlined by Kim et al. (2020). In brief, hydrothermal fluid in the OVF typically effuses from the fissures of basement rock, and no typical chimney structure is observed (Figure 1D). Around the OVF, small chimney fragments, altered rocks, and Fe-oxide crust are widely distributed in an area approximately 100–150 m in diameter. Numerous hydrothermal animals (21 macrofaunal taxa) have been observed on and around the diffuse vent, with a distribution range of

approximately 100 m in diameter from the vent; these animals include mussels, gastropods, crabs, shrimps, barnacles, and anemones. Rock samples dredged at the OVF have indicated that the basement rock of the vent field consists primarily of altered gabbroic and ultramafic (i.e., serpentinized-peridotite) sequences. Furthermore, breccia-type sulfides collected by rock dredges have displayed thin greenish layers of copper (Cu)-bearing secondary minerals. The plume over the OVF site is

particle-poor (e.g., max. $\Delta\text{NTU} = 0.002$ in particle anomaly), although it is characterized by a substantial oxidation-reduction potential anomaly ($\Delta E = -20$ mV at approximately 100 m above the bottom), with a corresponding increase in the total dissolved iron (Fe, 191 nM in maximum value), manganese (Mn, 1.5 nM in maximum value) and methane (CH_4 , 52.5 nM in maximum value). The average dissolved Fe/Mn and CH_4 /Mn ratios were 5.6 and 36.2, respectively, which are within the typical range of the mid-ocean ridge hydrothermal system (Kim et al., 2020 and reference therein).

MATERIALS AND METHODS

A total of 18 surface sediments were collected in and around the OVF using TV-grab and multiple box-core samplers on the cruises of R/V ISABU between 2017 and 2019 (Figure 1C). Angular, dark glossy volcanoclastic particles (pyroclastic shards, Lim et al., 2020, 2021) abundantly observed in some surface sediments were also collected for geochemical compositions. For geochemical compositions, sediment and volcanoclastic particle samples were freeze-dried and then ground using an agate mortar. The total nitrogen (TN), carbon (TC), and sulfur (TS) contents of these sediments were measured using an elemental analyzer (FLASH 2000, Thermo Fisher Scientific, Waltham, MA, United States), and the total inorganic carbon (TIC) content was measured using a CO_2 coulometer (model CM5014: UIC, Joliet, IL, United States) in the geochemistry laboratory of Library for Marine Samples (LIMS), Korea Institute of Ocean Science & Technology (KIOST). The analytical accuracy and precision of these elements were within 5%, based on an analysis of standard reference materials [L-cysteine for TN and TC analysis, BBOT for TS analysis, and pure calcium carbonate (CaCO_3) with 12.00 C% for TIC analysis] and replicated samples. TIC content was converted to CaCO_3 content as a weight percentage using a multiplication factor of 8.333, and total organic carbon (TOC) content was calculated from the difference between the TC and TIC contents.

For the concentration of 17 elements (SiO_2 , Al_2O_3 , Fe_2O_3 , MgO , CaO , Na_2O , K_2O , TiO_2 , MnO , Ba , Co , Cr , Cu , Ni , Pb , Sn , and Zn), each powdered sediment sample was fused with lithium metaborate (LiBO_2) flux and the molten beads were then poured into a volume of dilute nitric acid and stirred until dissolved (Lim et al., 2015). The resultant solutions were then analyzed using a combination of a Thermo ICAP 6500 radial inductively coupled plasma optical emission spectroscopy (ICP-OES) and Thermo Elemental X Series II ICP mass spectrometry (ICP-MS). Calibration for both instruments was achieved via matrix matched calibration standards produced from combinations of ICP-grade single element standards. The accuracy of the analytical method was monitored by repeated analysis of standard reference materials (ACE, OU6 and SBC-1, $n = 5$, respectively), together with a batch of sediment samples. The results showed that relative deviations between measured and certificated values were less than 5–10% in most elements (Supplementary Table 1). To gain detailed information about the origin and mode of occurrence of the elements in these surface

sediments, we analyzed the concentrations of the acid leachable fraction (hereafter the labile phase) of each sample, including the water-soluble, exchangeable, and acid-soluble phases (Cronan and Hodkinson, 1997; Song and Choi, 2009; Mascarenhas-Pereira and Nath, 2010). For element composition of the labile fraction, bulk sediment samples were leached with 1N hydrochloric acid (HCl) for 24 h at room temperature (Yang et al., 2004; Song and Choi, 2009), and then the supernatant (solution) was analyzed for the leached concentrations of 17 elements using ICP-OES and ICP-MS at Korea Basic Science Institute, Korea. Here, the elemental concentration of the residual fraction was defined as the difference between the total and labile fractions of bulk sediments.

The stable carbon isotope ($\delta^{13}\text{C}$) of organic matter and sulfur isotope ($\delta^{34}\text{S}$) of bulk sediments and hydrothermal minerals were measured using an Elemental Analyzer-Isotope Ratio Mass Spectrometer (EA-IRMS, Elementar GmbH, Langenselbold, Hesse, Germany), hosted at the LIMS, KIOST. Isotopic compositions were reported relative to conventional reference materials; Vienna Peedee Belemnite (VPDB) for carbon and Vienna Canyon Diablo Troilite (VCDT) for sulfur. The measured $\delta^{13}\text{C}$ for the carbonate-removed sediments were calibrated using international reference materials; IAEA-600, USGS40, USGS43, and IAEA-CH-6. For $\delta^{34}\text{S}$ composition, untreated samples were combusted with vanadium pentoxide (V_2O_5) and the measured $\delta^{34}\text{S}$ was calculated using international reference materials; IAEA-S1, IAEA-S2, and IAEA-SO6. All sediment samples, together with standard materials, were analyzed in duplicate or triplicate. Measurement reproducibility as determined from replicate analysis was less than approximately $\pm 0.04\text{‰}$ for $\delta^{13}\text{C}$ and $\pm 0.3\text{‰}$ for $\delta^{34}\text{S}$ (Supplementary Table 1).

For identifying hydrothermal minerals (i.e., barite and talc) found in surface sediments, the X-ray diffraction (XRD) data were collected with a Bruker D8 Advance A25 diffractometer using graphite-monochromatized $\text{CuK}\alpha$ radiation at Gyungsang National University, Korea; the mineral grains were collected from some surface sediments under the microscope and were then powdered for subsequent analysis. The samples were measured from 4° to 70° (2θ) at an interval of 0.02° step size with 0.2 s of time scan under the conditions of 40 kV/40 mA of accelerating voltage and $\text{CuK}\alpha$ (1.5418 \AA) radiation. Their morphologies and chemical compositions were taken using a JEOL JSM 7600F field emission scanning electron microscope (SEM) equipped with an energy dispersive x-ray spectrometer (EDS) at the LIMS, KIOST. The analyses were performed under the conditions of an acceleration voltage of 10–20 kV and a beam diameter of $3 \mu\text{m}$.

Strontium ($^{86}\text{Sr}/^{87}\text{Sr}$) isotope compositions of the barite grain samples ($n = 12$) were analyzed using a Neptune Plus multi-collector ICP-MS (MC-ICP-MS, Thermo Fisher Scientific, Waltham, MA, United States), coupled with a RESolution M-50 193 nm laser ablation system (Resonetics, Nashua, NH, United States), hosted at the State Key Laboratory of Isotope Geochemistry, Guangzhou Institute of Geochemistry, Chinese Academy of Sciences (GIG, CAS). The interferences of ^{84}Kr and ^{86}Kr on ^{84}Sr and ^{86}Sr were corrected by subtracting gas blank from the raw time-resolved signal intensities. ^{85}Rb

was used to correct the interference of ^{87}Rb on ^{87}Sr with a natural $^{85}\text{Rb}/^{87}\text{Rb} = 2.593$ (Catanzaro et al., 1969). The mass bias of $^{87}\text{Sr}/^{86}\text{Sr}$ was normalized to $^{86}\text{Sr}/^{88}\text{Sr} = 0.1194$ with an exponential law. The detailed data reduction procedure is reported in Zhang et al. (2018). Ten analyses of NKT-1G (a basaltic glass) during the course of this measurement yielded a weighted mean of $^{87}\text{Sr}/^{86}\text{Sr} = 0.70355 \pm 0.00009$ (2SD), which is consistent within error of the value reported in Elburg et al. (2005). Fifteen analyses of an in-house plagioclase glass (PZHPL) yielded a weighted mean of $^{87}\text{Sr}/^{86}\text{Sr} = 0.70435 \pm 0.00010$ (2SD), agreeing within error with the result measured by solution method (Zhang et al., 2019).

In this study, multivariate statistical approaches were applied to clarify the distribution of geochemical components and to better define the significant relationships between them. Statistical analyses were performed using Excel-XLSTAT (Version 2009.1.01).

RESULTS

Most surface sediments are composed of yellowish, foraminiferal nanofossiliferous ooze, frequently including angular, dark glossy volcanoclastic particles, except for the sediment samples proximal to the hydrothermal edifices of the OVF with low CaCO_3 contents. The analytical results for the geochemical compositions

of all sediments samples and their statistic summary are given in **Table 1** and **Supplementary Table 2**, respectively. The geochemical compositions of the sediments vary considerably depending on the sample site. TN, TOC, and TS contents range from 236 to 735 $\mu\text{g/g}$ (average: 433 $\mu\text{g/g}$), 1,947–5,941 $\mu\text{g/g}$ (average: 3,967 $\mu\text{g/g}$), and 1,110–19,177 $\mu\text{g/g}$ (average: 3,652 $\mu\text{g/g}$), respectively. The CaCO_3 contents are generally between 50 and 84%, excluding some samples with low contents (<10%) and agree with the total concentration of CaO, suggesting that the calcium in the sediments is derived largely from biogenic components (i.e., foraminiferal tests). Carbon and sulfur isotope compositions also exhibit a wide range; $\delta^{13}\text{C}$ of organic matter and $\delta^{34}\text{S}$ of bulk sediments ranged from -25.20 to -19.77‰ (average -21.35‰) and $+13.57$ to $+22.27\text{‰}$ (average: $+19.52\text{‰}$), respectively.

In total concentration, CaO (average: 30.65%, range: 0.25–48.16%) and SiO_2 (average: 23.33%, range: 4.84–68.81%) are the most abundant elements, followed by MgO, Fe_2O_3 , Na_2O , and Al_2O_3 with average values of 6.76% (range: 0.55–25.45%), 3.28% (range: 0.73–13.50%), 2.87% (range: 0.90–4.27%), and 2.22% (range: 0.65–7.50%), respectively. The concentrations of MnO, K_2O , and TiO_2 are generally low, ranging from 0.03 to 2.77% (average: 0.26%), 0.09 to 0.40% (average: 0.23%), and 0.00 to 0.36% (average: 0.10%), respectively. Of the trace elements, the concentrations of Ba (average: 6,026 $\mu\text{g/g}$, range: 466–41,101 $\mu\text{g/g}$) and Cu (average: 437 $\mu\text{g/g}$, range: 37–3,545 $\mu\text{g/g}$)

TABLE 1 | Descriptive statistics of elemental compositions for surface sediments of the study area.

Elements	OVF sediments (n = 18)				OVF volcanoclastic grains (n = 6)				*MORB	*Basalt (n = 26)				
	Total fraction		1 N leachable fraction		Average		SD		Average	Average				
	Average	SD	Min	Max	Average	SD	Min	Max	Average	Average				
TN ($\mu\text{g/g}$)	433	146	236	735	–	–	–	–	–	–				
TOC ($\mu\text{g/g}$)	3967	1020	1947	5941	–	–	–	–	–	–				
TS ($\mu\text{g/g}$)	3652	4675	1110	19177	–	–	–	–	–	–				
CaCO_3 (%)	51.1	29.4	0.1	83.6	–	–	–	–	–	–				
Al_2O_3 (%)	2.22	2.27	0.65	7.50	0.81	0.72	0.15	2.37	15.91	0.55	15.39	16.62	14.95	16.16
CaO (%)	30.65	16.63	0.25	48.16	29.94	16.74	0.22	47.97	11.41	0.15	11.24	11.67	11.39	–
Fe_2O_3 (%)	3.28	2.94	0.73	13.50	1.82	2.37	0.36	10.92	9.80	0.36	9.35	10.16	11.30	11.10
K_2O (%)	0.23	0.09	0.09	0.40	0.18	0.07	0.05	0.30	0.16	0.02	0.13	0.17	0.14	0.14
MgO (%)	6.76	8.18	0.55	25.45	1.47	0.87	0.47	2.79	7.64	0.14	7.53	7.86	7.69	8.38
MnO (%)	0.26	0.63	0.03	2.77	0.13	0.21	0.01	0.97	0.17	0.02	0.16	0.21	0.18	0.16
Na_2O (%)	2.87	0.89	0.90	4.27	2.71	0.83	0.81	4.23	2.60	0.04	2.57	2.66	2.76	2.39
SiO_2 (%)	23.33	19.20	4.84	68.81	1.69	1.00	0.72	5.07	49.39	0.37	48.93	49.92	50.41	48.95
TiO_2 (%)	0.10	0.11	0.00	0.36	0.02	0.03	0.00	0.09	1.39	0.03	1.35	1.43	1.68	1.10
Ba ($\mu\text{g/g}$)	6206	11577	466	41101	614	1288	21	5408	17	3	12	20	23	–
Co ($\mu\text{g/g}$)	15	11	4	44	9	8	1	29	43	3	41	49	43	49
Cr ($\mu\text{g/g}$)	81	118	2	444	17	21	0	78	409	121	300	627	251	230
Cu ($\mu\text{g/g}$)	437	879	37	3545	278	591	4	2292	67	4	61	72	75	93
Ni ($\mu\text{g/g}$)	60	71	7	225	26	28	0	95	124	17	115	158	97	143
Pb ($\mu\text{g/g}$)	42.5	87.8	1.7	334.2	31.9	65.6	1.5	230.7	2.8	2.1	1.0	6.9	0.5	2.0
Sr ($\mu\text{g/g}$)	4.09	8.80	0.16	34.91	2.20	4.88	0.00	19.48	1.07	0.15	0.89	1.30	0.79	–
Zn ($\mu\text{g/g}$)	74	109	16	478	43	68	12	311	84	6	77	91	87	95

*Data from MORB and basalt are from Gale et al. (2013) and Liao et al. (2019) respectively.

are highest, followed by Cr, Zn, Ni, and Pb, with averages of 81 $\mu\text{g/g}$ (range: 2–444 $\mu\text{g/g}$), 74 $\mu\text{g/g}$ (range: 16–478 $\mu\text{g/g}$), 60 $\mu\text{g/g}$ (range: 7–225 $\mu\text{g/g}$), and 43 $\mu\text{g/g}$ (range: 2–334 $\mu\text{g/g}$), respectively. Co and Sn are less than 45 and 35 $\mu\text{g/g}$ in maximum concentrations, respectively (**Table 1**). The relative proportion of the labile phase (1M HCl leachable fraction) compared with the total concentration was as high as 70% in average values for Ca, K, Mn, Na, and Pb, followed by Co, Cu, Fe, Mg, and Zn; the average ranges were 50–70%. In contrast, Ba, Cr, Si, and Ti were lower than 30% on average, suggesting that they mainly exist in acid-insoluble fractions (e.g., silicate and/or sulfate minerals).

Pure sand-sized volcanoclastic particles from some sediments are clearly distinguished from bulk sediments with respect to their elemental composition (**Table 1**). SiO_2 , Al_2O_3 , and CaO are the most abundant elements, with averages of 49.39% (range: 48.93–49.92%), 15.91% (range: 15.39–16.62%), and 11.41% (range: 11.24–11.67%), respectively, followed by Fe_2O_3 (average: 9.80%, range: 9.35–10.16%), MgO (average: 7.64%, range: 7.53–7.86%), Na_2O (average: 2.60%, range: 2.57–2.66%), TiO_2 (average: 1.39%, range: 1.35–1.43%), MnO (average: 0.17%, range: 0.16–0.21%), and K_2O (average: 0.16%, range: 0.13–0.17%). Among the trace elements, the average concentrations of Cr, Ni, and Zn reached 409 $\mu\text{g/g}$ (range: 300–627 $\mu\text{g/g}$), 124 $\mu\text{g/g}$ (range: 115–158 $\mu\text{g/g}$), and 84 $\mu\text{g/g}$ (range: 77–91 $\mu\text{g/g}$),

respectively. Other elements, including Co and Cu, were as low as 40–70 $\mu\text{g/g}$; Ba, Pb, and Sn were less than 20 $\mu\text{g/g}$. Characteristically, Al, Co, Cr, Fe, and Ti concentrations were much higher than those of the surface sediments of the OVF; however, Ba, Cu, K, Mn, Pb, and Sn concentrations were lower (**Table 1**).

DISCUSSION

Geochemical Characteristics of Mid-Ocean Ridge Sediments

The agglomerative hierarchical clustering (AHC) analysis grouped the surface sediments into three clusters (A, B1, and B2) on the basis of compositional similarity between the samples (**Figure 2A**). The sediments of group A, corresponding to the hydrothermal edifice of the OVF, were characterized by the highest concentrations of Fe, Mg, Mn, Si, Ba, Cu, Sn, Pb, and Zn (**Table 2**). Group B1, comprising of sediment samples around and distant from the OVF, had significantly higher in Al, K, Na, Ti, Cr, Co, and Ni concentrations. Another distal sediment group located far from the OVF (group B2) had the highest concentrations of Ca but the lowest concentrations of most other elements, possibly due to the carbonate dilution effect.

Identification of the hydrothermal components and their quantitative contributions in mid-ocean ridge sediments can be estimated using various elemental discrimination diagrams. For example, element ratios such as $\text{Al}/(\text{Al} + \text{Fe} + \text{Mn})$ and $(\text{Fe} + \text{Mn})/\text{Ti}$ have been successfully used as indicators

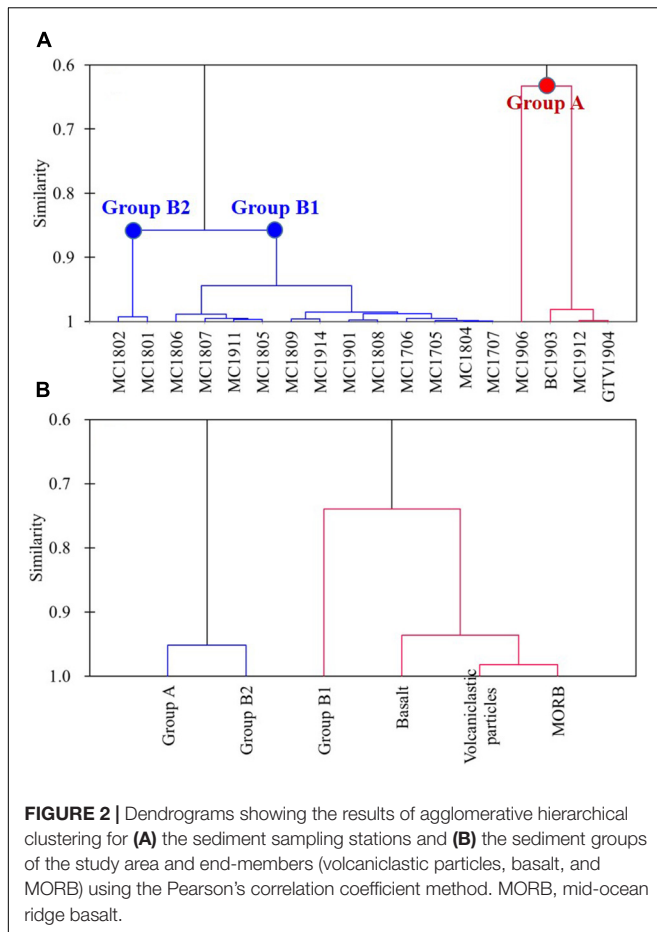


FIGURE 2 | Dendrograms showing the results of agglomerative hierarchical clustering for (A) the sediment sampling stations and (B) the sediment groups of the study area and end-members (volcanoclastic particles, basalt, and MORB) using the Pearson's correlation coefficient method. MORB, mid-ocean ridge basalt.

TABLE 2 | Average concentrations of elements for each sediment group of the study area, MORB, and basalt.

Elements	This study				*MORB	*Basalt
	Group A	Group B1	Group B2	Volcanoclastic particles		
Al_2O_3 (%)	1.19	2.80	0.78	15.91	14.95	16.16
CaO (%)	3.70	36.92	46.86	11.41	11.35	–
Fe_2O_3 (%)	5.63	2.89	0.97	9.80	11.30	11.10
K_2O (%)	0.14	0.26	0.22	0.16	0.14	0.14
MgO (%)	20.37	3.24	0.65	7.64	7.69	8.38
MnO (%)	0.72	0.13	0.13	0.17	0.17	0.16
Na_2O (%)	1.65	3.33	2.52	2.60	2.76	2.39
SiO_2 (%)	54.36	15.85	6.19	49.39	50.41	48.95
TiO_2 (%)	0.02	0.13	0.03	1.39	1.54	1.10
Ba ($\mu\text{g/g}$)	24590	947	987	17	23	–
Co ($\mu\text{g/g}$)	11	17	8	43	43	49
Cr ($\mu\text{g/g}$)	28	111	4	409	251	230
Cu ($\mu\text{g/g}$)	1566	124	57	67	75	93
Ni ($\mu\text{g/g}$)	25	79	15	124	97	143
Pb ($\mu\text{g/g}$)	170.4	5.8	6.5	2.8	0.5	2.0
Sn ($\mu\text{g/g}$)	17.06	0.41	0.21	1.07	0.79	–
Zn ($\mu\text{g/g}$)	212	38	19	84	87	95

*Data from MORB and basalt are from Gale et al. (2013) and Liao et al. (2019), respectively.

of hydrothermal sedimentation (e.g., Marchig et al., 1982; Boström, 1983; Chen et al., 2004; Dias and Barriga, 2006; Slack et al., 2009; He et al., 2016; Liao et al., 2018b). The metalliferous index, calculated as $Al/(Al + Fe + Mn)$, is helpful for distinguishing hydrothermal components in various sediments; for instance, the ratio decreases with increasing hydrothermal input. Generally, pelagic deep-sea sediments have a metalliferous index of >0.4 , but metal-enriched sediments are less than 0.4 in this index (Boström, 1973, 1983). As shown in **Figure 3A**, all studied sediment samples plotted on the mixing line of the hydrothermal sediments (e.g., modern metalliferous sediments) and non-hydrothermal components (e.g., modern pelagic sediment, MORB, and upper continental crust)—the decreasing Fe/Ti ratio and increasing $Al/(Al + Fe + Mn)$ ratio indicate that most sediments of the study area are mixtures of hydrothermal-pelagic-volcanic components (e.g., Dias and Barriga, 2006; Liao et al., 2018b). The sediments of group A are within a typical metalliferous hydrothermal domain [$Al/(Al + Fe + Mn)$ ratio of <0.2] (**Figure 3A**); the high hydrothermal affinity in these OVF sediments is also evident in the Al–Fe–Mn ternary plot (**Figure 3B**). In addition, the Si/Al ratio is much higher in the sediments of group A (Si/Al of 27–70), compared with other groups that exhibited Si/Al ratios of 4–10, further supporting that these sediments are products of intense hydrothermal sedimentation from the OVF (Dias and Barriga, 2006). Meanwhile, the sediments of group B have a wide range of $Al/(Al + Fe + Mn)$ ratios from ~ 0.2 to 0.6, depending on the relative influence of the hydrothermal plume components. Hydrothermal sediments from the Rodrigues Triple Junction of CIR with the ratio of ~ 0.25 are geochemically most similar to some sediments of group B with relatively strong hydrothermal influence (**Figures 3A,B**). In group B1, characteristically, some sediments (samples MC1706, MC1809, MC1705, and MC1914,

Figure 1C) have much higher ratios of $Al/(Al + Fe + Mn)$ (>0.4), which are close to the values of MORB as well as volcanoclastic particles. This result is also supported by the Al–Fe–Mn ternary plot (**Figure 3B**), suggesting that these sediments are predominantly composed of non-hydrothermal components (especially volcanic debris). Subsequently, the sediments of group A represent pronounced hydrothermal components of the OVF, while the group B1 sediments are mixtures of hydrothermal sediments and volcanic materials. Considering the low TOC, TS, and high $CaCO_3$ contents, the sediments of group B2 are primarily composed of typical calcareous pelagic sediments, including some hydrothermal components (Liao et al., 2019). The AHC analysis for average elemental concentrations of each sediment group and non-hydrothermal end-members (i.e., volcanoclastic particles, MORB, and upper continental crust) also supports this conclusion (**Figure 2B**). Besides, the overall elemental compositions of these volcanoclastic particles are similar to those of MORB and basalts. Therefore, the elemental composition of volcanoclastic particles collected from the studied samples is considered as end-member component of the ridge volcanism, which is representative of the MORB composition in the CIR. Here, we have established a set of element indicators for hydrothermal or volcanic sedimentation, including discrimination diagrams, which can be employed to more accurately estimate the source of elements, and thus to better understand the characteristic of hydrothermal vent fluid, especially in the ancient deep-sea ridge deposits.

Controlling Factors of Elemental Compositions

Principal component analysis in this study revealed three key components that explained 87% of the total variance (**Table 3**).

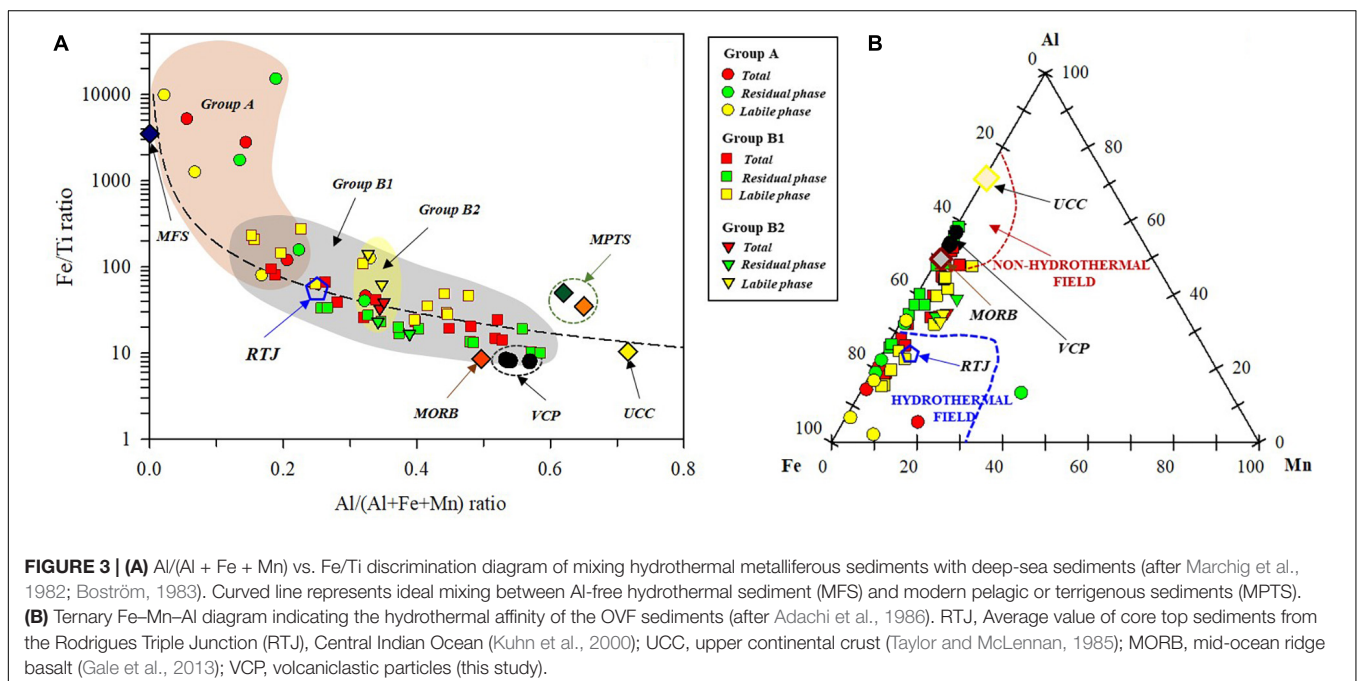


TABLE 3 | Results of principal component analysis for the sediment dataset and percentage of variance explained for the individual factor loadings (>0.5 value).

	Factor 1	Factor 2	Factor 3
Eigenvalue	9.8	5.4	3.2
Variability (%)	35	25	28
TN ($\mu\text{g/g}$)	0.65	-0.06	0.61
TOC ($\mu\text{g/g}$)	0.05	0.12	0.71
TS ($\mu\text{g/g}$)	0.96	-0.20	-0.04
CaCO ₃ (%)	-0.82	-0.29	-0.46
Al ₂ O ₃ (%)	-0.01	0.95	-0.05
CaO (%)	-0.84	-0.22	-0.47
Fe ₂ O ₃ (%)	0.14	0.35	0.90
K ₂ O (%)	-0.52	0.54	-0.03
MgO (%)	0.91	0.05	0.39
MnO (%)	-0.03	-0.03	0.94
Na ₂ O (%)	-0.73	0.45	-0.13
SiO ₂ (%)	0.85	0.16	0.32
TiO ₂ (%)	-0.09	0.90	-0.15
Ba ($\mu\text{g/g}$)	0.96	-0.22	0.09
Cr ($\mu\text{g/g}$)	0.04	0.92	-0.06
Cu ($\mu\text{g/g}$)	0.29	-0.13	0.93
Ni ($\mu\text{g/g}$)	-0.04	0.88	0.04
Zn ($\mu\text{g/g}$)	0.32	-0.02	0.94
Co ($\mu\text{g/g}$)	-0.08	0.94	0.25
Pb ($\mu\text{g/g}$)	0.43	-0.19	0.87
Sn ($\mu\text{g/g}$)	0.94	-0.16	0.07

Factor 1 (35% of the total variance) was highlighted by high positive loadings for TS, Si, Mg, Ba, and Sn, which are largely enriched in the sediments of group A (i.e., the OVF hydrothermal sediments). The high concentrations of SiO₂ (45–68%) and MgO (14–25%), as well as the good affinity ($r^2 = 0.80$) between these elements, imply the presence of hydrothermal phyllosilicate minerals (e.g., talc and serpentine). Indeed, the presence of talc {[Mg₃Si₄O₁₀(OH)₂], 63.5% SiO₂, 31.7% MgO, and 4.8% H₂O} in the OVF deposits was confirmed by XRD and SEM analyses (Figures 4A–F, 5A). Bulk XRD analyses of the massive, globular, and white-colored aggregates (up to 5 mm in size, Figures 4A–C) separated from the group A sediments showed peaks at approximately 9.6 Å (for the 001 plane) and 4.7 Å, confirming talc as the dominant phase (Figure 5A). SEM observations also revealed that these minerals are characterized by predominant platy and flaky texture, resulting in the formation of boxwork- or honeycomb-like structures (Figures 4D,E). SEM-EDS microanalysis of two talc granules ($n = 33$ points) yielded the following average composition results (Figure 4F): 53.6 ± 4.4% (39.0–58.6%) of Si, 33.2 ± 3.7% (24.9–38.2%) of Mg, 9.7 ± 6.7% (3.3–34.2%) of Fe, 2.3 ± 0.5% (1.1–3.4%) of Al, 0.7 ± 1.4% (0.0–3.9%) of Cu, and 0.5 ± 0.4% (0.2–2.2%) of Ca. Si and Mg contents at >85% and the high Si/Mg molar ratio (average: 1.41, range: 1.24–1.72)—which is close to or slightly higher than that of pure magnesian talc (1.33)—demonstrated that the talc invariably has an almost pure end-member composition. The slightly higher Si/Mg ratios may be associated with the amorphous silica (>95% in SiO₂, opal-A) frequently observed inside talc (Supplementary

Figures 1A–C). Accordingly, the abundant occurrence of talc is reflected in the whole sediment geochemistry by the high concentrations of Si and Mg.

Another remarkable feature of Factor 1 is the presence of significant correlations among TS, Ba, and Sn, suggesting that they are mainly derived from hydrothermal barites (BaSO₄, Figures 4G–L, 5B); the importance of this mineral is discussed in section “Hydrothermal Barite.” This preliminary result demonstrated that hydrothermal minerals have a substantial effect on these elemental concentrations and spatial distributions. Notably, CaCO₃, Ca, K, and Na with high negative loadings may be highly dependent on the amounts of the biogenic components and/or seawaters included in the sediments (Table 3). The labile phase of these elements comprises more than 90% of the total concentration and is uniform across all sediments without spatial distribution trend.

Factor 2 (25% of the total variance) exhibited significant positive component loadings for Al, Co, Cr, K, Ni, and Ti (Table 3), as well as good correlations among them (Supplementary Figure 2). Their concentrations were significantly higher in the sediments of group B1 (Table 2), including volcanoclastic particles commonly dispersed in mid-ocean ridge sediments. As discussed above, these particles from the study area are characterized by significantly higher Al, Cr, Ni, and Ti concentrations, as well as lower K concentrations, compared with the surrounding sediments. On the basis of K₂O/TiO₂ ratio (average: 0.11), the volcanoclastic particles from the study area may correspond to the transitional MORB (Marty and Zimmermann, 1999). Therefore, the elemental components of Factor 2 may result from a contribution of volcanic materials (e.g., pyroclastic shard particles) from the ridge volcanism around the OVF (Kuhn et al., 2000; Lim et al., 2020, 2021; Chen et al., 2021).

Factor 3 (28% of the total variance) showed positive loadings for TN, TOC, Fe, Mn, Cu, Pb, and Zn; their concentrations are highest in group A (Tables 2, 3). Considering the excellent covariation among them (Supplementary Figure 2) and the increased enrichment of the elements in the sediments of group A proximal to the vent field, hydrothermal-derived materials (e.g., Fe–Mn oxyhydroxides and/or sulfides associated with organic matter) may be the primary controlling factor in the concentrations of these elements and their spatial distributions (Chen et al., 2021). However, biogenic and volcanic influences on these elements are generally minor. In conclusion, the OVF hydrothermal sediments (group A) are characterized by high concentrations of TS, Si, Mg, and Ba derived from talc and barite minerals, as well as Fe, Mn, and some trace elements from the Fe–Mn oxides and/or sulfides; but, Al, K, Na, Ti, Co, Ni, and Cr are likely from ridge volcanisms.

Stable Carbon and Sulfur Isotopes

The $\delta^{13}\text{C}$ and $\delta^{34}\text{S}$ values of the surface sediments in the study area show a distinct difference between the sediment groups (Figure 6). The $\delta^{13}\text{C}$ in the hydrothermal sediments of group A (–25.20 to –22.47‰) exhibit lighter isotope values, compared with the sediments of group B (–21.29 to –19.77‰), within the range of marine plankton (–22 to –20‰, Imbus et al., 1992;

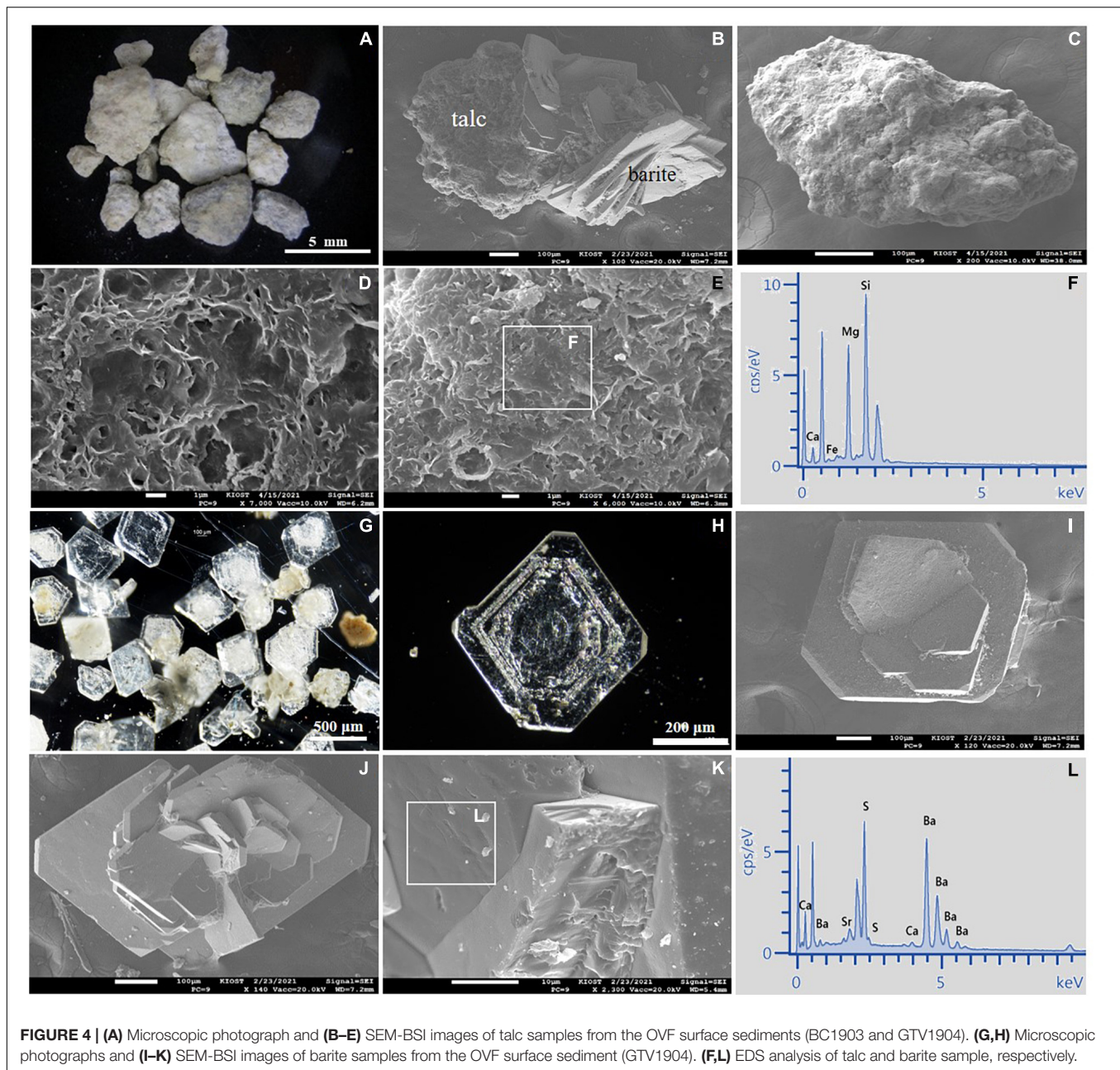
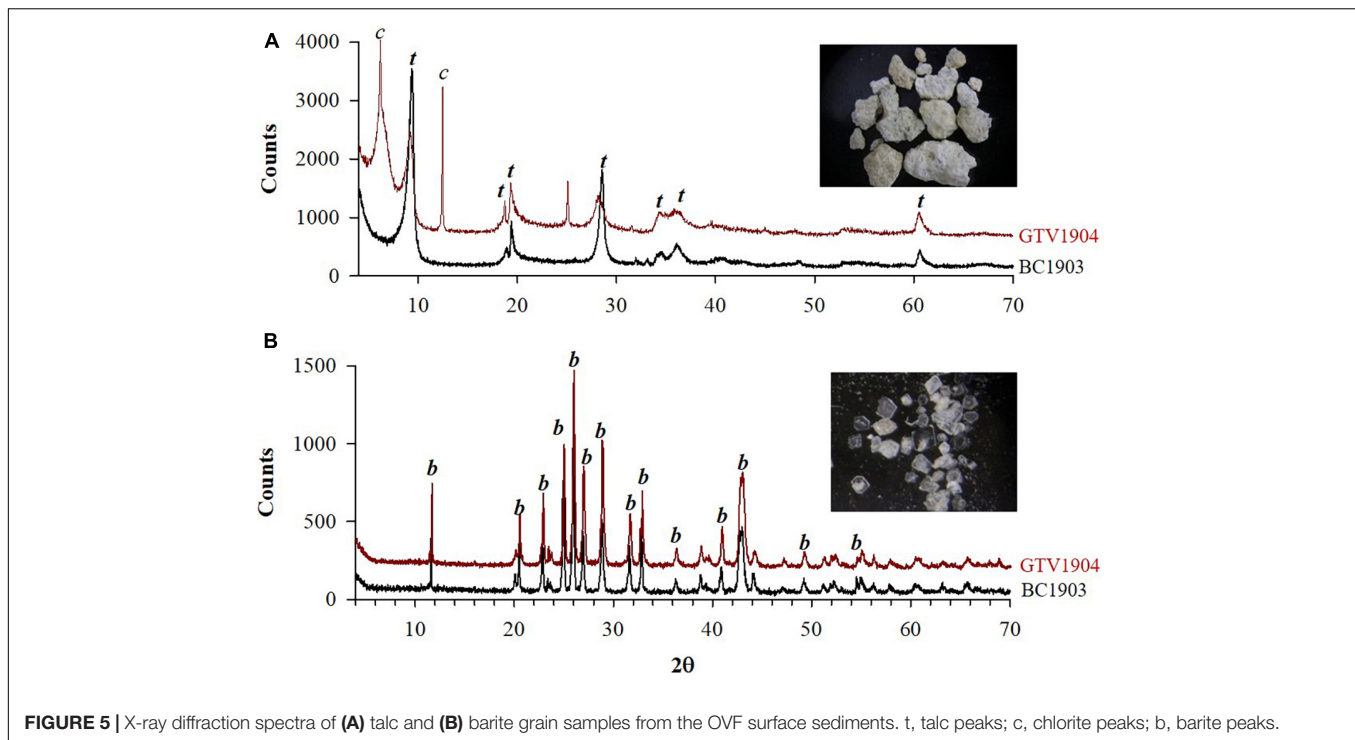


FIGURE 4 | (A) Microscopic photograph and (B–E) SEM-BSI images of talc samples from the OVF surface sediments (BC1903 and GTV1904). (G,H) Microscopic photographs and (I–K) SEM-BSI images of barite samples from the OVF surface sediment (GTV1904). (F,L) EDS analysis of talc and barite sample, respectively.

Walinsky et al., 2009). The $\delta^{13}\text{C}$ values of hydrothermal vent fluid for CH_4 at the East Pacific Rise and the southern Juan de Fuca ridge ranged from -20.8 to -15.0‰ and -50.8 to -43.2‰ at the Guaymas Basin (Shanks et al., 1995 and reference therein). In contrast, the $\delta^{13}\text{C}$ values of the hydrothermal vent fluid for CO_2 are mostly higher than approximately -10‰ (Shanks et al., 1995 and references therein; Shanks, 2001). Thus, the lower $\delta^{13}\text{C}$ value in the hydrothermal sediments—particularly compared with the value in marine plankton—suggests some contributions of organic carbon from the benthic fauna that depend on methane-oxidizing (methanotrophic) metabolism (Kennicutt et al., 1992). This interpretation is also confirmed by the sulfur isotopic

composition and a close linkage ($r^2 = 0.78$) between the $\delta^{13}\text{C}$ and $\delta^{34}\text{S}$ values (Figure 6).

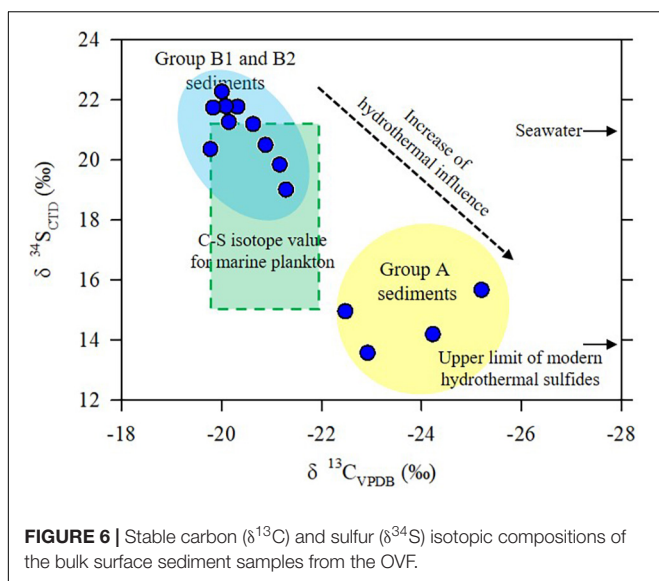
In the sediments of group B with a comparatively low S/C ratio (<0.5), the $\delta^{34}\text{S}$ value ranged from $+19$ to $+23\text{‰}$ (average: $+21.03\text{‰}$), corresponding to the values of present-day seawater ($+21.0 \pm 0.2\text{‰}$, Rees et al., 1978) and marine phytoplankton ($+15$ to $+20\text{‰}$, Shanks et al., 1995), which assimilate sulfate; however, the $\delta^{34}\text{S}$ value of the group B sediments is much higher than that of bacteriogenic pyrite (approximately -15‰ , Krouse, 1980; Kaplan, 1983). Assimilatory reduction occurs in autotrophic organisms where sulfur is incorporated in proteins, particularly as S^{2-} in amino-acids, the bonding of the produced



sulfur is similar to the dissolved sulfate ion, and fractionations are small (+0.5 to -4.5% , Kaplan, 1983). Considering that the $\delta^{34}\text{S}$ value of organic sulfur in extant marine organisms incorporated by assimilatory processes is generally depleted by 0–5‰ relative to the ocean (Paytan and Gray, 2012), most sulfur in the sediments of group B appears to exist as organosulfur compounds by the biological assimilation of seawater sulfate (Oduro et al., 2012).

Importantly, the $\delta^{34}\text{S}$ values (+13 to +15‰) of the hydrothermal sediments (group A) of the OVF are significantly

depleted, compared with the group B sediments. The $\delta^{34}\text{S}$ values of group A are much higher than those of basaltic oceanic crust (-1 to $+1\%$, Shanks et al., 1995), but are similar to or slightly higher than the upper limit value of the compositional range (-7.0 to $+13.8\%$, mostly -0.8 to $+10.2\%$) of primary sulfides from modern mid-ocean ridge hydrothermal fields (Melekestseva et al., 2014 and references therein; Fan et al., 2021 and references therein). In the study area, moreover, $\delta^{34}\text{S}$ values decrease as TS contents increase ($r^2 = 0.5$). In hydrothermal vent areas of mid-ocean ridges, most sulfur occurs predominantly as sulfide minerals, which often formed as the result of biogenic processes, and to a lesser extent, as organically bound sulfur. The biogenic processes are dominated by reduction during early diagenesis of seawater sulfate to form sulfides (e.g., pyrite) by sulfur-reducing bacteria, resulting in substantial isotopic fractionation, which ranges from 15 to 60‰ (average: 40‰, Shanks et al., 1995; Peters et al., 2011), leading to negative $\delta^{34}\text{S}$ values (e.g., Alt and Shanks, 2011). In most sediment-starved mid-ocean ridges, moreover, hydrothermal sulfides with basaltic sulfur as the principal source have $\delta^{34}\text{S}$ values from 0 to $+7\%$ (Herzig et al., 1998; Shanks, 2001). Thus, the lighter sulfur isotopic composition in the sediments of group A with high TS contents indicates a sulfur contribution from hydrothermal sulfides with the relatively low $\delta^{34}\text{S}$ value that is closely linked to bacterial sulfate reduction of seawater and/or thermochemical sulfate reduction. A comparatively very high sulfur/carbon ratio (1–6) in this group further supports the contribution of hydrothermal sulfide (Imbus et al., 1992). The relatively low $\delta^{34}\text{S}$ value in the sediments of group A, accordingly, reflects the mixed contribution of isotopically depleted sulfides (e.g., bacteriogenic pyrite) and enriched marine biomass (e.g.,



organosulfur compounds). Considering the abundant occurrence of barite with $\delta^{34}\text{S}$ similar to seawater (details provided in section “Hydrothermal Barite”), the sulfate mineral may act in the direction of increasing $\delta^{34}\text{S}$ value. Our finding reveals that paired carbon-sulfur isotopic compositions along with the elemental signature are useful precursors for better recognition of hydrothermal input in deep-sea sediments; the hydrothermal sediments are characterized by much lighter values in all stable isotopes, compared with the surrounding deep-sea sediments and seawater.

Hydrothermal Barite

Barite with a transparent, tubular form and a high degree of crystallinity was abundantly present in some hydrothermal sediments of group A (Figures 4G,H, 5B). In hydrothermal environments, in general, pure barite is formed by the mixture of vent fluid and seawater (Paytan et al., 2002; Eickmann et al., 2014; Jamieson et al., 2016; Zhang et al., 2020), and its isotope compositions cannot fractionate during and after crystallization (Paytan et al., 1993). Thus, the occurrence of barite in the surface sediments represents direct evidence of the OVF hydrothermal activity; furthermore, its chemical-isotopic compositions provide insights for better characterizing this hydrothermal system. To our knowledge, there have been no reports of barite in the Indian ridge hydrothermal fields. SEM observation has shown that barites occur in a typical rosette morphology consisting of tabular or plate crystals with mainly hexagonal forms, with sizes varying from approximately 100–500 μm (Figures 4I–K). EDS microanalysis to achieve chemical characterization of barite ($n = 22$ points in two representative barite grains) has shown average contents of $76.5 \pm 3.0\%$ (72.6–80.8%) for Ba, $19.0 \pm 2.8\%$ (15.0–22.3%) for S, and $4.1 \pm 1.0\%$ (2.3–5.2%) for Sr (Figure 4L). More than 90% of barite consists of Ba and S, and the Ba/S molar ratio of the samples (average: 1.07, range: 0.83–1.30) is close to that of pure barite.

Eickmann et al. (2014) proposed a scheme for differentiating the various mechanisms of barite precipitation based on sulfur and strontium isotope compositions, and we added our results to their dataset (Figure 7). The $\delta^{34}\text{S}$ values of the OVF barite samples ranged from +21.2 to +23.0‰ (average $+22.3 \pm 0.5\%$, $n = 20$ barite samples), which are comparable with, but slightly higher than, $\delta^{34}\text{S}$ value of present-day seawater ($+21.0 \pm 0.2\%$, Rees et al., 1978). However, these values are much lower than those of diagenetic barites (+24 to +59‰, Paytan et al., 2002), although they are more radiogenic than hydrothermal fluid (approximately 0‰) (Figure 7). In principle, the $\delta^{34}\text{S}$ value (e.g., +16.1 to +16.7‰, Herzig et al., 1998) of barite associated with the sulfides should be significantly lighter than that of seawater. As presented above, the $\delta^{34}\text{S}$ values of barite are higher than those of group A hydrothermal sediments containing some sulfide minerals, but are similar to those of the group B sediments (average: $+21.0 \pm 0.9\%$) that are related with the organosulfur compounds by the biological assimilation of seawater sulfate. There is increasing evidence that barite precipitation induced by hydrothermal activity yields $\delta^{34}\text{S}$ values that are similar to or slightly lower than the value of seawater sulfate (Paytan et al., 2002; De Ronde et al., 2003; Eickmann et al., 2014); however,

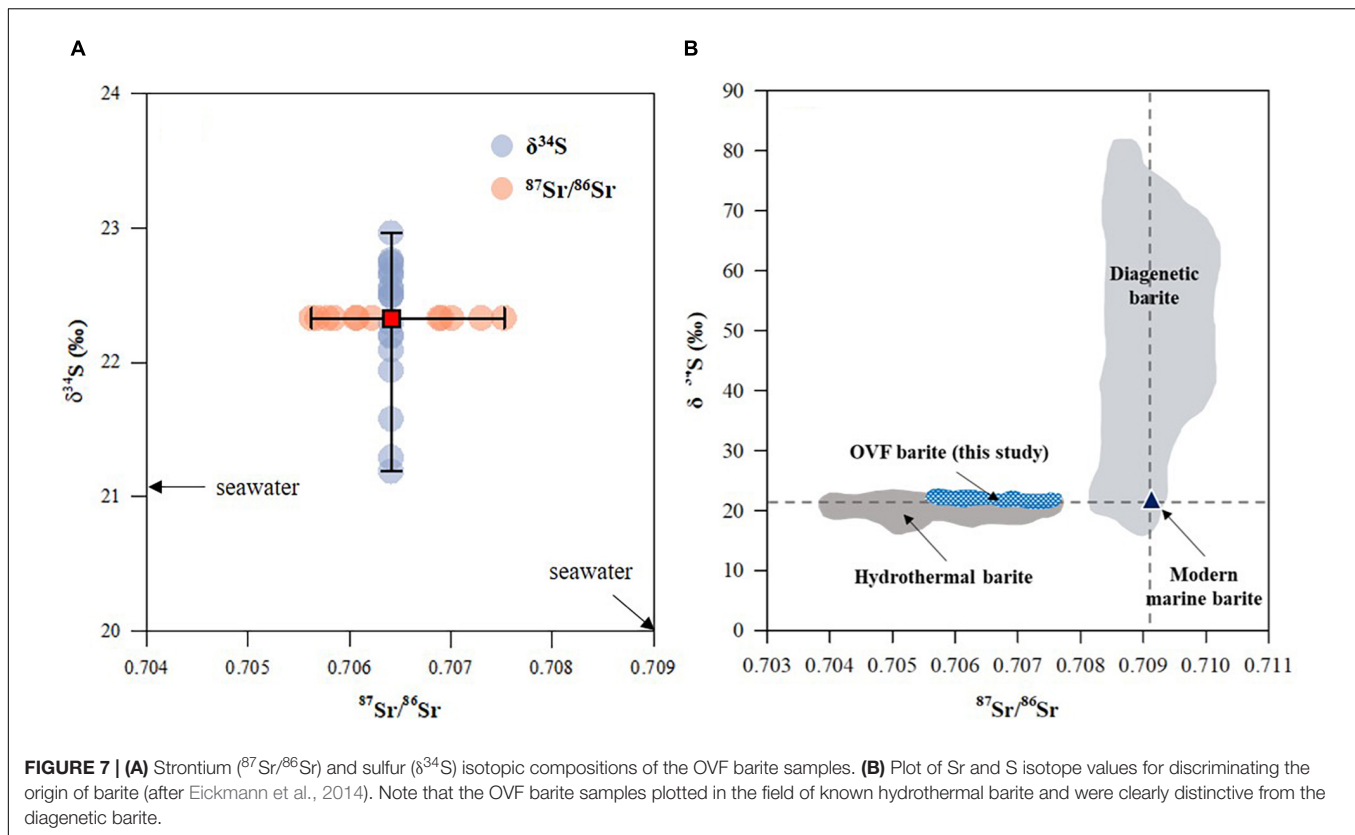
barite that precipitates from fluids modified by microbial sulfate reduction exhibits higher $\delta^{34}\text{S}$ values than the value of seawater sulfate (Wortmann et al., 2007; Feng and Roberts, 2011; Griffith and Paytan, 2012). Therefore, the results indicate that barite precipitation in the OVF may result from the hydrothermal reduction of seawater sulfate accompanied by the isotopic enrichment of the residual sulfate (Shanks et al., 1995) and/or involvement of weak biogenic processes in barite formation (Paytan et al., 2002).

To identify the origin of Ba in barite and to further confirm a hydrothermal contribution, the Sr isotopic ($^{87}\text{Sr}/^{86}\text{Sr}$) composition in barite grains was examined. The $^{87}\text{Sr}/^{86}\text{Sr}$ values of barites ranged from 0.70569 to 0.70753 (average: 0.70641 ± 0.00067), although most barite samples were within the range of 0.70606–0.70753. This range is slightly lower than the value of seawater (0.70917, Butterfield et al., 2001) and surface sediments from the CIR (average: 0.70944, range: 0.70810–0.71027, Anand et al., 2019), but is considerably higher than the ranges of CIR and Southwest Indian Ridge basalts (average: 0.70285 ± 0.00029 and 0.70494 ± 0.00037 , respectively, Michard and Albarède, 1986) and volcanic glass samples (0.70297, Price et al., 1986). As presented in Figure 7, the $^{87}\text{Sr}/^{86}\text{Sr}$ values of the OVF barites overlap with those of other hydrothermal barites that have distinctive Sr isotope values that are much less radiogenic than seawater (Eickmann et al., 2014). In general, the Sr isotope compositions of barites from sediment-free hydrothermal fields are between those of basement rocks and seawater. In contrast, barites from the thick sediment-covered hydrothermal field have an unusually higher $^{87}\text{Sr}/^{86}\text{Sr}$ value (0.71284–0.71749, Zhang et al., 2020) than seawater and associated basement rock, indicating interactions between hydrothermal fluid and local sediments. Therefore, the strontium isotope composition of barites from the sediment-free OVF hydrothermal field, which lies between the compositions of seawater and MORB or peridotite (Figure 7), reflects the sufficient fluid/seawater interaction in this region.

Based on simple mixing calculation using the Sr contents and isotopic values of end-members (seawater, gabbro, and barite), the relative contributions of hydrothermal fluid and seawater in the mixing fluid were estimated by applying a simple two-component mixing model as follows (Kuhn et al., 2003; Zhang et al., 2020):

$$\text{HF}(\%) = 100 \times \frac{\text{Sr}_{\text{SW}}((^{86}\text{Sr}/^{87}\text{Sr})_{\text{SW}} - (^{86}\text{Sr}/^{87}\text{Sr})_{\text{BA}})}{(\text{Sr}_{\text{SW}}((^{86}\text{Sr}/^{87}\text{Sr})_{\text{SW}} - (^{86}\text{Sr}/^{87}\text{Sr})_{\text{BA}}) + \text{Sr}_{\text{HF}}((^{86}\text{Sr}/^{87}\text{Sr})_{\text{BA}} - (^{86}\text{Sr}/^{87}\text{Sr})_{\text{HF}}))}$$

where HF (%) is the proportion of hydrothermal fluid, and Sr_{SW} and Sr_{HF} are Sr concentrations of seawater ($89.9 \mu\text{mol kg}^{-1}$; Gallant and Von Damm, 2006) and hydrothermal fluid, respectively. The $(^{86}\text{Sr}/^{87}\text{Sr})_{\text{SW}}$, $(^{86}\text{Sr}/^{87}\text{Sr})_{\text{BA}}$, and $(^{86}\text{Sr}/^{87}\text{Sr})_{\text{HF}}$ are Sr isotope ratios for seawater (0.70917), barite, and hydrothermal fluid, respectively. For Sr concentration and isotopic ratio of hydrothermal fluid, values of the ultramafic-hosted Kairei hydrothermal fluid ($75.3 \mu\text{mol kg}^{-1}$, Gallant and Von Damm, 2006) and the gabbro from the CIR (0.70287,



Ray et al., 2011) near the study area, respectively, were used. The results showed that the average contribution of hydrothermal fluid is estimated to be approximately 50% (range: 30–60%), even though there are uncertainties in values of hydrothermal fluid, implying that the physiochemical condition of mixing fluid changes considerably during the mineralization process. From such isotopic signatures, we concluded that the OVF hydrothermal barite was a primary precipitate from Ba-rich hydrothermal fluid mixed with seawater, which contrasts to marine barite precipitated in the water column and diagenetic barite precipitated at the oxic-anoxic boundary within sediments in association with sulfate-reducing conditions.

Characteristics of Onnuri Vent Field Hydrothermal System

The off-axis, ultramafic-hosted OVF has been primarily considered to be a low-temperature diffuse venting system (Kim et al., 2020). However, our results, together with plume chemistry data, suggest that the OVF has the characteristic of a high-temperature venting system with a weak or no magmatic heat source. Hydrothermal vent fluids associated with serpentinization of upper mantle peridotite are typically characterized by unusually high concentrations of abiogenic H_2 and CH_4 , a high CH_4/Mn ratio, and much lower dissolved silicate concentrations, compare with basalt-hosted hydrothermal system (Donval et al., 1997; Kelley et al., 2001; Charlou et al.,

2002 and references therein). In particular, the serpentinization reaction, especially at OCCs distant from the ridge axis, is capable of driving non-volcanic hydrothermal circulation (e.g., Rona et al., 1987; Grácia et al., 2000; Lowell and Rona, 2002; Kelley et al., 2005; Dias and Barriga, 2006; Hodgkinson et al., 2015). It is likely to occur in the OVF hydrothermal system hosted by serpentinized-peridotites and gabbros exposed by detachment faults; manifestation of such extensive reaction in this vent field can be inferred from the high CH_4 enrichment, high CH_4/Mn ratio, and negligible dissolved metal concentration in the vent plume (Kim et al., 2020). This nature of OVF system is better characterized by the massive occurrence and geochemistry of typical talc and barite minerals from hydrothermal sediments.

Considering the predominant occurrence of fragile talc granules with pure end-composition and boxwork-like microstructure, as well as other results (i.e., minor occurrence of sulfide minerals, absence of magnesite, and absence of sediment cover), the talc presumably precipitates directly from Si-rich hydrothermal fluids that seep out directly from the serpentinized-peridotites/gabbro reaction zone, rather than originating from the hydrothermal alteration of ultramafic rocks including the serpentinite (D’Orazio et al., 2004; Dias and Barriga, 2006; Hodgkinson et al., 2015). This prediction is further supported by the $^{87}\text{Sr}/^{86}\text{Sr}$ ratios (0.706156–0.707549, $n = 6$, Lim et al. unpublished data) for the talc samples from the OVF, which are similar to (but slightly less than) the ratio of present-day seawater (0.70917) and the Von Damm

Vent Field talc samples (0.706313–0.709168, Hodgkinson et al., 2015) that precipitated directly as a result of mixing between vent fluid and seawater. This implies that a substantial component of seawater was mixed with the vent fluids during the talc precipitation. Moreover, a manifestation of such direct precipitation of talc from the fluids mixed with seawater at the vent may be inferred from the presence of amorphous silica (**Supplementary Figures 1C,D**); for instance, Hodgkinson et al. (2015) proposed the possibility of instantaneous precipitation of talc and silica as the primary phases in mixing the hot (~215°C) vent fluid with cold seawater in the Von Damm Vent Field. At the OVF, the low metal content of the fluid may only result in accessory amounts of metal sulfides, possibly allowing talc to become the dominant phase. In many respects (e.g., geological conditions conducive to serpentinization, CH₄-rich fluid composition, and talc-dominated mineral deposits), the OVF system is comparable with the Von Damm, Lost City, St. Paul F.Z., and Saldanha hydrothermal vent fields, which are representative hydrothermal systems driven by the serpentinization reaction (Kelley et al., 2001, 2005; D'Orazio et al., 2004; Dias and Barriga, 2006; Hodgkinson et al., 2015). Accordingly, the precipitation of talc mineral is linked to the activity of the serpentinite/gabbro-hosted hydrothermal system, indicating that talc-dominated vent deposits may be considered an indicator of active off-axis hydrothermal fields, possibly sustained by serpentinization in the slow- and ultra-slow spreading CIR ridges where the basaltic magma flux is weakest.

Although the high CH₄ concentration suggests that serpentinization of the ultramafic rocks comprising the OVF basement has influenced fluid composition, the precipitation of barite indicates that the OVF hydrothermal fluids were likely influenced by interaction with mafic rocks (e.g., gabbro). Overall the ultramafic-hosted hydrothermal systems appear to be generally poor in Ba and barite because the Ba released from the hydrothermal leaching of ultramafic rocks is considerably limited, thereby resulting in precipitation of barite-free mineral assemblages (Noguchi et al., 2011; Melekestseva et al., 2014). This was also corroborated in seawater/peridotite thermodynamic reaction model and experimental studies, demonstrating that the ultramafic-hosted hydrothermal system cannot produce significant barite precipitates (Melekestseva et al., 2014 and references therein). Therefore, a mafic origin for the OVF barite appears most likely and is consistent with the presence of gabbroic rocks that were commonly dredged in and around the vent site. As discussed above, such evidence also exists for the talc formation, which is closely linked to interactions with Si-rich hydrothermal fluids, representing mafic components derived from interactions with gabbroic rocks within a peridotite-dominated ridge segment.

Accumulated evidence from several hydrothermal deposits, including the Grimsey and Guaymas Vent Fields, has revealed that the estimated temperature of talc formation in the hydrothermal environments is typically within the range of 250–370°C (Koski et al., 1985; D'Orazio et al., 2004 and references therein; Boschi et al., 2008; Dekov et al., 2008 and references therein). Considering these previous results, the

talc-dominated OVF may be a comparatively high-temperature hydrothermal system; this is also roughly consistent with the barite precipitation condition (approximately 240°C at maximum temperature, Melekestseva et al., 2014). This is supported, to some extent, by the abundant occurrence of breccia-type sulfides with Cu-bearing secondary minerals in the OVF, indicative of episodically higher vent temperatures (e.g., >200°C, Kim et al., 2020). In fact, this speculation is confirmed by the temperature (160–250°C, Lim et al. unpublished data) measured in the subsurface sediment layer (5 cm in sediment depth) of the OVF region using ROV. This high temperature of the OVF vent fluid is approximately equal to the temperature of heat released from the exothermic serpentinization reaction (150–250 °C, Batch et al., 2002; Alt et al., 2007; Boschi et al., 2008). However, the low fluid temperature at the escape orifices (~4–12°C, Lim et al., unpublished data) is probably a consequence of cooling effects during conductive circulation and seawater interactions in the diffuse vent system; in general, many hydrothermal fields include both high-temperature vents in the center and low-temperature vents near the perimeter (e.g., Dias and Barriga, 2006; Chen et al., 2018 and reference therein). Subsequently, the occurrence of barite and talc minerals in the hydrothermal sediments support that the OVF is a high temperature hydrothermal circulation system driven by serpentinization. Furthermore, this conclusion suggests that the serpentinization process can heat up circulating water to >200°C, even though some authors argued that this process does not produce enough heat to explain peridotite-hosted hydrothermal systems (e.g., Batch et al., 2002; Lowell and Rona, 2002; Allen and Seyfried, 2003).

CONCLUSION

Considering the presence of serpentinized-peridotite, a strong methane anomaly, an apparent lack of a magmatic heat source, and the predominant occurrence of talc and barite, we conclude that the serpentinization of exposed mantle rocks along the detachment faults likely plays a key role in the OVF hydrothermal circulation. Unlike the early study that described the OVF as a low-temperature hydrothermal venting system, our results reveal that the studied diffuse vent is the high-temperature system of >200°C. Considering the widespread occurrence of OCCs in the CIR, the OVF may be a representative off-axis peridotite-hosted hydrothermal system in the CIR, characterized by talc-dominated mineralization. Our study yields important geochemical data regarding hydrothermal sediments and minerals that provide a unique perspective on the ultramafic-hosted hydrothermal system in an off-axis OCC setting with a non-magmatic heat source, which was previously poorly investigated in the CIR.

DATA AVAILABILITY STATEMENT

The original contributions presented in the study are included in the article/**Supplementary Material**, further inquiries can be directed to the corresponding author/s.

AUTHOR CONTRIBUTIONS

DL and JoK contributed to conception and design of the study and wrote the first draft of the manuscript. LZ, KK, and JiK performed the analyses and organized the data. All authors contributed to manuscript revision, read, and approved the submitted version.

FUNDING

This work was supported by the Ministry of Oceans and Fisheries, South Korea, as part of the project titled ‘Understanding the deep-sea biosphere on seafloor hydrothermal vents in the Indian Ridge’ (Grant Number 20170411), the National Research Foundation of Korea (NRF) grant (2021R1A2C1014443) funded by the Ministry of Science and ICT of Korea government and the

REFERENCES

- Adachi, M., Yamamoto, K., and Sugisaki, R. (1986). Hydrothermal cherts and associated silicious rocks from northern Pacific: their geological significance as indication of ocean ridge activity. *Sed. Geol.* 47, 125–148. doi: 10.1016/0037-0738(86)90075-8
- Allen, D. E., and Seyfried, W. E. Jr. (2003). Compositional controls on vent fluids from ultramafic-hosted hydrothermal systems at mid-ocean ridges: an experimental study at 400°C, 500 bars. *Geochim. Cosmochim. Acta* 67, 1531–1542. doi: 10.1016/S0016-7037(02)01173-0
- Alt, J. C., and Shanks, W. C. (2011). Microbial sulfate reduction and the sulfur budget for a complete section of altered oceanic basalts, IODP Hole 1256D (eastern Pacific). *Earth Planet. Sci. Lett.* 310, 73–83. doi: 10.1016/j.epsl.2011.07.027
- Alt, J. C., Shanks, W. C., Bach, W., Paulick, H., Garrido, C. J., and Beaudoin, G. (2007). Hydrothermal alteration and microbial sulfate reduction in peridotite and gabbro exposed by detachment faulting at the Mid-Atlantic Ridge, 15°20'N (ODP Leg 209): A sulfur and oxygen isotope study. *Geochem. Geophys. Geosyst.* 8:Q08002. doi: 10.1029/2007GC001617
- Anand, S. S., Rahaman, W., Lathika, N., Thamban, M., Patil, S., and Mohan, R. (2019). Trace Elements and Sr, Nd Isotope Compositions of Surface Sediments in the Indian Ocean: An Evaluation of Sources and Processes for Sediment Transport and Dispersal. *Geochem. Geophys. Geosyst.* 20, 3090–3112. doi: 10.1029/2019GC008332
- Batch, W., Garrido, C. J., Paulick, H., Harvey, J., and Rosner, M. (2002). Seawater-peridotite interactions: First insights from ODP Leg 209, MAR 15°N. *Geochem. Geophys. Geosyst.* 5:Q09F26. doi: 10.1029/2004GC000744
- Beaulieu, S., Baker, E. T., and German, C. R. (2015). Where are the undiscovered hydrothermal vents on oceanic spreading ridges? *Deep Sea Res. Part II* 121, 202–212. doi: 10.1016/j.dsr2.2015.05.001
- Beaulieu, S., Baker, E. T., German, C. R., and Maffei, A. (2013). An authoritative global database for active submarine hydrothermal vent fields. *Geochem. Geophys. Geosyst.* 14, 4892–4905. doi: 10.1002/2013GC004998
- Boschi, C., Dini, A., Früh-Green, G. L., and Kelley, D. S. (2008). Isotopic and element exchange during serpentinization and metasomatism at the Atlantis Massif (MAR 30°N): Insights from B and Sr isotope data. *Geochim. Cosmochim. Acta* 72, 1801–1823. doi: 10.1016/j.gca.2008.01.013
- Boström, K. (1973). The origin and fate of ferromanganous active ridge sediments. *Stockh. Contrib. Geol.* 27, 149–243.
- Boström, K. (1983). “Genesis of Ferromanganese Deposits—Diagnostic Criteria for Recent and Old Deposits,” in *Hydrothermal Processes at Seafloor Spreading Centers*, ed. P. A. Rona (Berlin: Springer), 473–489. doi: 10.1007/978-1-4899-0402-7_20
- Butterfield, D. A., Nelson, B. K., Wheat, C. G., Mottl, M., and Roe, K. (2001). Evidence for basaltic Sr in mid ocean ridge flank hydrothermal systems and implications for the global oceanic Sr isotope balance. *Geochim. Cosmochim. Acta* 65, 4141–4153. doi: 10.1016/S0016-7037(01)00712-8
- Catanzaro, E. J., Murphy, T. J., Garner, E. L., and Shields, W. R. (1969). Absolute isotopic abundance ratio and atomic weight of terrestrial rubidium. *J. Res. Natl. Bur. Stand. A* 73, 511–516. doi: 10.6028/jres.073A.041
- Cave, R. R., German, C. R., Thomson, J., and Nesbitt, R. W. (2002). Fluxes to sediments underlying the Rainbow hydrothermal plume at 36°14'N on the Mid-Atlantic Ridge. *Geochim. Cosmochim. Acta* 66, 1905–1923. doi: 10.1016/S0016-7037(02)00823-2
- Charlou, J. L., Donval, J. P., Fouquet, Y., Jean-Baptiste, P., and Holm, N. (2002). Geochemistry of high H₂ and CH₄ vent fluids issuing from ultramafic rocks at the Rainbow hydrothermal field (36°14'N, MAR). *Mar. Geol.* 191, 345–359. doi: 10.1016/S0009-2541(02)00134-1
- Chen, J. F., Sun, S. L., Liu, W. H., and Zheng, J. J. (2004). Geochemical characteristics of organic matter-rich strata of lower Cambrian in Tarim Basin and its origin. *Sci. China Ser. D Earth Sci.* 47, 125–132. doi: 10.1360/04zd0031
- Chen, J., Tao, C., Liang, J., Liao, S., Dong, C., Li, H., et al. (2018). Newly discovered hydrothermal fields along the ultraslow spreading Southwest Indian Ridge around 63°E. *Acta Oceanol. Sin.* 37, 61–67. doi: 10.1007/s13131-018-1333-y
- Chen, X., Sun, X., Wu, Z., Wang, Y., Lin, X., and Chen, H. (2021). Mineralogy and geochemistry of deep-sea sediments from the ultraslow-spreading Southwest Indian Ridge: Implications for hydrothermal input and igneous host rock. *Minerals* 11:138. doi: 10.3390/min11020138
- Choi, S. K., Park, S. J., Kim, J., Park, J.-W., and Son, S.-K. (2021). Gold and tin mineralisation in the ultramafic-hosted Cheoem vent field, Central Indian Ridge. *Miner. Deposita* 56, 885–906. doi: 10.1007/s00126-020-01012-5
- Cronan, D. S., and Hodkinson, R. A. (1997). Geochemistry of hydrothermal sediments from ODP Sites 834 and 835 in the Lau Basin, southwest Pacific. *Mar. Geol.* 141, 237–268. doi: 10.1016/S0025-3227(97)00071-6
- D’Orazio, M., Boschi, C., and Brunelli, D. (2004). Talc-rich hydrothermal rocks from the St. Paul and Conrad fracture zones in the Atlantic Ocean. *Eur. J. Mineral.* 16, 73–83. doi: 10.1127/0935-1221/2004/0016-0073
- De Ronde, C. E. J., Faure, K., Bray, C. J., Chappell, D. A., and Wright, I. C. (2003). Hydrothermal fluids associated with seafloor mineralization at two southern Kermadec arc volcanoes, offshore New Zealand. *Miner. Deposita* 38, 217–233. doi: 10.1007/s00126-002-0305-4
- Dekov, V., Boycheva, T., Halenius, U., Billstrom, K., Kamenov, G. D., Shanks, W. C., et al. (2011). Mineralogical and geochemical evidence for hydrothermal activity at the west wall of 12°50'N complex (Mid-Atlantic ridge): a new ultramafic-hosted seafloor hydrothermal deposit? *Mar. Geol.* 283, 90–102.
- Dekov, V. M., Cuadros, J., Shanks, W. C., and Koski, R. A. (2008). Deposition of talc—kerolite—smectite — smectite at seafloor hydrothermal vent fields: Evidence from mineralogical, geochemical and oxygen isotope studies. *Chem. Geol.* 247, 171–194. doi: 10.1016/j.chemgeo.2007.10.022

Strategic Priority Research Program of the Chinese Academy of Sciences (XDB42000000 and XDB40010100).

ACKNOWLEDGMENTS

We sincerely thank scientists and crews of the RV/LISABU for their support during the sampling and data collection. We would also like to appreciate the reviewers whose comments allowed us to greatly improve this manuscript.

SUPPLEMENTARY MATERIAL

The Supplementary Material for this article can be found online at: <https://www.frontiersin.org/articles/10.3389/fmars.2022.810949/full#supplementary-material>

- Dias, A. A., and Barriga, F. J. A. S. (2006). Mineralogy and geochemistry of hydrothermal sediments from the serpentinite-hosted Saldanha hydrothermal field (36°34'N; 33°26'W) at MAR. *Mar. Geol.* 225, 157–175. doi: 10.1016/j.margeo.2005.07.013
- Donval, J. P., Charlou, J. L., Douville, E., Knoery, J., Fouquet, Y., Poncevera, E., et al. (1997). High H₂ and CH₄ content in hydrothermal fluids from Rainbow site newly sampled at 36°14'N on the AMAR segment, Mid-Atlantic Ridge (diving FLORES cruise, July 1997): Comparison with other MAR sites. *EOS Trans. Am. Geophys. Union* 78:V51.
- Eickmann, B., Thorseth, I. H., Peters, M., Strauss, H., Brocker, M., and Pedersen, R. B. (2014). Barite in hydrothermal environments as a recorder of seafloor processes: A multiple isotope study from the Loki's Castle vent field. *Geobiology* 12, 308–321. doi: 10.1111/gbi.12086
- Elburg, M., Vroon, P., Wagt, B. V. D., and Tchalikian, A. (2005). Sr and Pb isotopic composition of five USGS glasses (BHVO-2G, BIR-1G, BCR-2G, TB-1G, NKT-1G). *Chem. Geol.* 223, 196–207. doi: 10.1016/j.chemgeo.2005.07.001
- Fan, L., Wang, G., Holzheid, A., Zoheir, B., and Shi, X. (2021). Sulfur and copper isotopic composition of seafloor massive sulfides and fluid evolution in the 26°S hydrothermal field, Southern Mid-Atlantic Ridge. *Mar. Geol.* 435:106436. doi: 10.1016/j.margeo.2021.106436
- Feng, D., and Roberts, H. (2011). Geochemical characteristics of the barite deposits at cold seeps from the northern Gulf of Mexico. *Earth Planet. Sci. Lett.* 309, 89–99. doi: 10.1016/j.epsl.2011.06.017
- Gale, A., Dalton, C. A., Langmuir, C. H., Su, Y., and Schilling, J.-G. (2013). The mean composition of ocean ridge basalt. *Geochem. Geophys. Geosyst.* 14, 489–518. doi: 10.1029/2012GC004334
- Gallant, R. M., and Von Damm, K. L. (2006). Geochemical controls on hydrothermal fluids from the Kairei and Edmond Vent Fields, 23°–25°S, Central Indian Ridge. *Geochem. Geophys. Geosyst.* 7:Q06018. doi: 10.1029/2005GC001067
- German, C. R., and Seyfried, W. E. Jr (2014). “Hydrothermal processes,” in *Treatise on Geochemistry*, Vol. 8, eds H. D. Holland and K. K. Turekian (Oxford: Elsevier), 191–233. doi: 10.1016/B978-0-08-095975-7.00607-0
- German, C. R., Baker, E. T., Mevel, C., Tamaki, K., and the Fuji Scientific Team. (1998). Hydrothermal activity along the Southwest Indian Ridge. *Nature* 395, 490–493. doi: 10.1038/26730
- Grácia, E., Charlou, J. L., Radford-Knoery, J., and Parson, M. (2000). Non-transform offsets along the Mid-Atlantic Ridge south of the Azores (38°N–34°N): Ultramafic exposures and hosting of hydrothermal vents, Earth Planet. Sci. Lett. 177, 89–103. doi: 10.1016/S0012-821X(00)00034-0
- Griffith, E. M., and Paytan, A. (2012). Barite in the ocean—occurrence, geochemistry and palaeoceanographic applications. *Sedimentology* 59, 1817–1835. doi: 10.1111/j.1365-3091.2012.01327.x
- Hannington, M., Jamieson, J., Monecke, T., Petersen, S., and Beaulieu, S. (2011). The abundance of seafloor massive sulfide deposits. *Geology* 39, 1155–1158. doi: 10.1130/G32468.1
- He, C., Ji, L., Wu, Y., Su, A., and Zhnag, M. (2016). Characteristics of hydrothermal sedimentation process in the Yanchang Formation, south Ordos Basin, China: Evidence from element geochemistry. *Sediment. Geol.* 345, 33–41. doi: 10.1016/j.sedgeo.2016.09.001
- Herzig, P. M., Hannington, M. D., and Arribas, A. Jr. (1998). Sulfur isotopic composition of hydrothermal precipitates from the Lau back-arc: implications for magmatic contributions to sea-floor hydrothermal systems. *Miner. Deposita* 33, 226–237. doi: 10.1007/s001260050143
- Hodgkinson, M. R. S., Webber, A. P., Roberts, S., Mills, R. A., Connelly, D. P., and Murton, B. J. (2015). Talc-dominated seafloor deposits reveal a new class of hydrothermal system. *Nat. Commun.* 6:10150. doi: 10.1038/ncomms10150
- Imbus, S. W., Macko, S. A., Elmore, R. D., and Engel, M. H. (1992). Stable isotope (C, S, N) and molecular studies on the Precambrian Nonesuch Shale (Wisconsin-Michigan, U.S.A.): Evidence for differential preservation rates, depositional environment and hydrothermal influence. *Chem. Geol.* 101, 255–281. doi: 10.1016/0009-2541(92)90007-R
- Jamieson, J. W., Hannington, M. D., Tivey, M. K., Hansteen, T., Williamson, N. M. B., Stewart, M., et al. (2016). Precipitation and growth of barite within hydrothermal vent deposits from the endeavour segment, Juan de Fuca Ridge. *Geochim. Cosmochim. Acta* 173, 64–85. doi: 10.1016/j.gca.2015.10.021
- Kaplan, I. R. (1983). “Stable isotopes of sulfur, nitrogen and deuterium in recent marine environments,” in *Stable Isotopes in Sedimentary Geology*, ed. M. A. Arthur (Oklahoma, OK: SEPM Society for Sedimentary Geology), 1–108.
- Kelley, D. S., Karson, J. A., Blackman, D. K., Fruh-Green, G. L., Butterfield, D. A., Lilley, M. D., et al. (2001). An off-axis hydrothermal vent field near the Mid-Atlantic Ridge at 30°N. *Nature* 412, 145–149. doi: 10.1038/35084000
- Kelley, D. S., Karson, J. A., Fruh-Green, G. L., Yoerger, D., Shank, T. M., Butterfield, D. A., et al. (2005). A serpentinite-hosted ecosystem: The Lost City Hydrothermal Field. *Science* 307, 1428–1434. doi: 10.1126/science.1102556
- Kennicutt, M. C., Burke, R. A., Macdonald, I. R., Brooks, J. M., Denoux, G. J., and Macko, S. A. (1992). Stable isotope partitioning in seep and vent organisms—chemical and ecological significance. *Chem. Geol.* 101, 293–310. doi: 10.1016/0009-2541(92)90009-T
- Kim, J., Son, S. -K., Kim, D., Pak, S. J., Yu, O. H., Walker, S. L., et al. (2020). Discovery of active hydrothermal vent fields along the Central Indian Ridge, 8–12°S. *Geochem. Geophys. Geosyst.* 21:e2020GC009058. doi: 10.1029/2020GC009058
- Koski, R. A., Lonsdale, P. F., Shanks, W. C., Berndt, M. E., and Howe, S. S. (1985). Mineralogy and geochemistry of a sediment-hosted hydrothermal sulfide deposit from the Southern Trough of Guaymas Basin, Gulf of California. *J. Geophys. Res.* 90, 6695–6707. doi: 10.1029/JB090iB08p06695
- Krouse, H. R. (1980). “Sulphur isotopes in our environment,” in *Handbook of Environmental Isotope Geochemistry*, eds P. Fritz and J. C. Fontes (Amsterdam: Elsevier), 435–471. doi: 10.1016/B978-0-444-41780-0.50017-1
- Kuhn, T., Burger, H., Castradori, D., and Halbach, P. (2000). Volcanic and hydrothermal history of ridge segments near the Rodrigues Triple Junction (Central Indian Ocean) deduced from sediment geochemistry. *Mar. Geol.* 169, 391–409. doi: 10.1016/S0025-3227(00)00080-3
- Kuhn, T., Herzig, P. M., Hannington, M. D., Garbe-Schönberg, D., and Stoffers, P. (2003). Origin of fluids and anhydrite precipitation in the sediment-hosted Grimsey hydrothermal field north of Iceland. *Chem. Geol.* 202, 5–21. doi: 10.1016/S0009-2541(03)00207-9
- Liao, S., Tao, C., Dias, A. A., Su, X., Yang, Z., Ni, J., et al. (2019). Surface sediment composition and distribution of hydrothermal derived elements at the Duanqiao-1 hydrothermal field, Southwest Indian Ridge. *Mar. Geol.* 416, 105975. doi: 10.1016/j.margeo.2019.105975
- Liao, S., Tao, C., Li, H., Barriga, F. J. A. S., Liang, J., Yang, W., et al. (2018a). Bulk geochemistry, sulfur isotope characteristics of the Yuhuang-1 hydrothermal field on the ultraslow-spreading Southwest Indian Ridge. *Ore Geol. Rev.* 96, 13–27. doi: 10.1016/j.oregeorev.2018.04.007
- Liao, S., Tao, C., Li, H., Zhang, G., Liang, J., Yang, W., et al. (2018b). Surface sediment geochemistry and hydrothermal activity indicators in the Dragon Horn area on the Southwest Indian Ridge. *Mar. Geol.* 398, 22–34. doi: 10.1016/j.margeo.2017.12.005
- Lim, D. I., Xu, Z., Choi, J., Li, T., and Kim, S. (2015). Holocene changes in detrital sediment supply to the eastern part of the central Yellow Sea and their forcing mechanisms. *J. Asian Ear. Sci.* 105, 18–31. doi: 10.1016/j.jseas.2015.03.032
- Lim, D., Kim, H., Kim, J., Jeong, D., and Kim, D. (2020). Mercury proxy for hydrothermal and submarine volcanic activities in the sediment cores of Central Indian Ridge. *Mar. Pollut. Bull.* 159:111513. doi: 10.1016/j.marpolbul.2020.111513
- Lim, D., Kim, J., Kim, J., Kim, D., Jeong, D., Kim, H., et al. (2021). Enhancement of volcanic eruption in mid-ocean ridge system during the last deglaciation: new sedimentary evidence in the Central Indian Ridge. *Mar. Geol.* 440:106574. doi: 10.1016/j.margeo.2021.106574
- Lowell, R. P., and Rona, P. A. (2002). Seafloor hydrothermal systems driven by the serpentinization of peridotite. *Geophys. Res. Lett.* 29:1531. doi: 10.1029/2001GL014411
- Marchig, V., Gundlach, H., Möller, P., and Schley, F. (1982). Some geochemical indicators for discrimination between diagenetic and hydrothermal metalliferous sediments. *Mar. Geol.* 50, 241–256. doi: 10.1016/0025-3227(82)90141-4
- Marty, B., and Zimmermann, L. (1999). Volatiles (He, C, N, Ar) in mid-ocean ridge basalts: assessment of shallow-level fractionation and characterization of source composition. *Geochim. Cosmochim. Acta* 63, 3619–3633. doi: 10.1016/S0016-7037(99)00169-6
- Mascarenhas-Pereira, M. B. L., and Nath, B. N. (2010). Selective leaching studies of sediments from a seamount flank in the Central Indian basin: resolving

- hydrothermal, volcanogenic and terrigenous components using major, trace and rare-earth elements. *Mar. Chem.* 121, 49–66. doi: 10.1016/j.marchem.2010.03.004
- Melekestseva, I. Y., Tret'yakov, G. A., Nimis, P., Yuminov, A. M., Maslennikov, V. V., Maslennikova, S. P., et al. (2014). Barite-rich massive sulfides from the Semenov-1 hydrothermal field (Mid-Atlantic Ridge, 13°30.87' N): Evidence for phase separation and magmatic input. *Mar. Geol.* 349, 37–54. doi: 10.1016/j.margeo.2013.12.013
- Michard, A., and Albarède, F. (1986). The REE content of some hydrothermal fluids. *Chem. Geol.* 55, 51–60. doi: 10.1016/0009-2541(86)90127-0
- Nakamura, K., and Takai, K. (2015). “Indian Ocean Hydrothermal Systems: Seafloor Hydrothermal Activities, Physical and Chemical Characteristics of Hydrothermal Fluids, and Vent-Associated Biological Communities,” in *Subseafloor biosphere linked to hydrothermal systems*, eds J. Ishibashi, et al. (Berlin: Springer), 147–162. doi: 10.1007/978-4-431-54865-2_12
- Nakamura, K., Watanebe, H., Miyazaki, J., Takai, K., Kawagucci, S., Noguchi, T., et al. (2012). Discovery of new hydrothermal activity and chemosynthetic fauna on the Central Indian Ridge at 18°–20°S. *PLoS One* 7:e32965. doi: 10.1371/journal.pone.0032965
- Noguchi, T., Shinjo, R., Ito, M., Takada, J., and Oomori, T. (2011). Barite geochemistry from hydrothermal chimneys of the Okinawa Trough: Insight into chimney formation and fluid/sediment interaction. *J. Miner. Petrol. Sci.* 106, 26–35. doi: 10.2465/jmps.090825
- Oduro, H., Von Alstyn, K. L., and Farquhar, J. (2012). Sulfur isotope variability of oceanic DMSP generation and its contributions to marine biogenic sulfur emissions. *Proc. Natl. Acad. Sci.* 109, 9012–9016. doi: 10.1073/pnas.1117691109
- Park, S. J., Moon, J. W., Kim, J., Chandler, M. T., Kim, H. S., Son, J., et al. (2017). Widespread tectonic extension at the Central Indian Ridge between 8°S and 18°S. *Gondwana Res.* 45, 163–179. doi: 10.1016/j.gr.2016.12.015
- Paytan, A., and Gray, E. T. (2012). “Sulfur Isotope Stratigraphy,” in *The Geologic Time Scale*, eds F. M. Gradstein, J. G. Ogg, M. Schmitz, and G. Ogg (Berlin: Elsevier), 167–179. doi: 10.1016/B978-0-444-59425-9.00009-3
- Paytan, A., Kastner, M., Martin, E. E., Macdougall, J. D., and Herbert, T. (1993). Marine barite as a monitor of seawater strontium isotope composition. *Nature* 366, 445–449. doi: 10.1038/366445a0
- Paytan, A., Mearon, S., Cobb, K., and Kastner, M. (2002). Origin of marine barite deposits: Sr and S isotope characterization. *Geology* 30, 747–750. doi: 10.1130/0091-7613(2002)030<0747:OOMBDS>2.0.CO;2
- Peters, M., Strauss, H., Petersen, S., Kummer, N.-A., and Thomazo, C. (2011). Hydrothermalism in the Tyrrhenian Sea: Inorganic and microbial sulfur cycling as revealed by geochemical and multiple sulfur isotope data. *Chem. Geol.* 280, 217–231. doi: 10.1016/j.chemgeo.2010.11.011
- Price, R. C., Kennedy, A. K., Riggs-Sneeringer, M., and Frey, F. A. (1986). Geochemistry of basalts from the Indian Ocean triple junction: implications for the generation and evolution of Indian Ocean ridge basalts. *Ear. Planet. Sci. Lett.* 78, 379–396. doi: 10.1016/0012-821X(86)90005-1
- Ray, D., Misra, S., Banerjee, R., and Weis, D. (2011). Geochemical implications of gabbro from the slow-spreading Northern Central Indian Ocean Ridge, Indian Ocean. *Geol. Mag.* 148, 404–422. doi: 10.1017/S001675681000083X
- Rees, C. E., Jenkins, W. J., and Monster, J. (1978). The sulphur isotope geochemistry of ocean water sulphate. *Geochim. Cosmochim. Acta* 42, 377–382. doi: 10.1016/0016-7037(78)90268-5
- Rona, P. A., Widenfalk, L., and Bostrom, K. (1987). Serpentinized ultramafics and hydrothermal activity at the Mid-Atlantic Ridge crest near 15°N. *J. Geophys. Res.* 92, 1417–1427. doi: 10.1029/JB092iB02p01417
- Shanks, W. C. (2001). “Stable isotopes in seafloor hydrothermal systems: vent fluids, hydrothermal deposits, hydrothermal alteration, and microbial processes,” in *Stable Isotope Geochemistry*, eds J. W. Valley and D. R. Cole (Washington D.C.: Mineralogical Society of America), 469–517. doi: 10.1515/9781501508745-011
- Shanks, W. C., Bohlke, J. K., and Seal, R. R. (1995). “Stable Isotopes in Mid-Ocean Ridge Hydrothermal Systems: Interactions between Fluids, Minerals, and Organisms,” in *Seafloor Hydrothermal Systems: Physical, Chemical, Biological, and Geological Interactions*, eds S. E. Humphris, R. A. Zierenberg, L. S. Mullineaux, and R. E. Thomson (Washington, DC: American Geophysical Union), 194–221. doi: 10.1029/GM091p0194
- Slack, J. F., Grenne, T., and Bekker, A. (2009). Seafloor hydrothermal Si-Fe-Mn exhalites in the Pecos greenstone belt, New Mexico, and the redox state of ca. 1720 Ma deep seawater. *Geosphere* 5, 302–314. doi: 10.1130/GES00220.1
- Son, J., Pak, S. J., Kim, J., Baker, E. T., You, O. R., Son, S. K., et al. (2014). Tectonic and magmatic control of hydrothermal activity along the slow-spreading Central Indian Ridge, 8°S–17°S. *Geochem. Geophys. Geosyst.* 15, 2011–2020. doi: 10.1002/2013GC005206
- Song, Y. H., and Choi, M. S. (2009). REE geochemistry of fine-grained sediments from major rivers around the Yellow sea. *Chem. Geol.* 266, 328–342. doi: 10.1016/j.chemgeo.2009.06.019
- Suo, Y., Li, S., Li, X., Zhang, Z., and Ding, D. (2017). The potential hydrothermal systems unexplored in the Southwest Indian Ocean. *Mar. Geophys. Res.* 38, 61–70. doi: 10.1007/s11001-016-9300-5
- Tao, C., Lin, J., Guo, S., Chen, Y. J., Wu, G., Han, X., et al. (2012). First active hydrothermal vents on an ultraslow-spreading center: Southwest Indian Ridge. *Geology* 40, 47–50. doi: 10.1130/G32389.1
- Taylor, S. R., and McLennan, S. M. (1985). *The Continental Crust: its Composition and Evolution*. New York, NY: Oxford University Press.
- Tivey, M. K. (2007). Generation of seafloor hydrothermal vent fluids and associated mineral deposits. *Oceanography* 20, 50–65. doi: 10.5670/oceanog.2007.80
- Walinsky, S. E., Prah, F. G., Mix, A. C., Finney, B. P., Jaeger, J. M., and Rosen, G. P. (2009). Distribution and composition of organic matter in surface sediments of coastal Southeast Alaska. *Cont. Shelf Res.* 29, 1565–1579. doi: 10.1016/j.csr.2009.04.006
- Wang, T., Chen, Y. J., and Tao, C. (2011). Revisit the K-segment of the Southeast Indian Ridge for new evidence of hydrothermal plumes. *Chin. Sci. Bull.* 56, 3605–3609. doi: 10.1007/s11434-011-4723-5
- Wortmann, U. G., Chernyavsky, B. M., Bernasconi, S. M., Brunner, B., Böttcher, M. E., and Swart, P. K. (2007). Oxygen isotope biogeochemistry of pore water sulfate in the deep biosphere: dominance of isotope exchange reactions with ambient water during microbial sulfate reduction (ODP Site 1130). *Geochim. Cosmochim. Acta* 71, 4221–4232. doi: 10.1016/j.gca.2007.06.033
- Yang, S. Y., Lim, D. I., Jung, H. S., and Oh, B. C. (2004). Geochemical composition and provenance discrimination of coastal sediments around Cheju Island in the southeastern Yellow Sea. *Mar. Geol.* 206, 41–53. doi: 10.1016/j.margeo.2004.01.005
- Zhang, L., Ren, Z.-Y., Handler, M. R., Wu, Y.-D., Zhang, L., Qian, S.-P., et al. (2019). The origins of high-Ti and low-Ti magmas in large igneous provinces, insights from melt inclusion trace elements and Sr-Pb isotopes in the Emeishan large Igneous Province. *Lithos* 344–345, 122–133. doi: 10.1016/j.lithos.2019.06.014
- Zhang, L., Ren, Z.-Y., Wu, Y.-D., and Li, N. (2018). Strontium isotope measurement of basaltic glasses by laser ablation multiple collector inductively coupled plasma mass spectrometry based on a linear relationship between analytical bias and Rb/Sr ratios. *Rapid Commun. Mass Spectrom.* 32, 105–112. doi: 10.1002/rcm.8011
- Zhang, X., Zhai, S. K., and Yu, Z. H. (2020). Strontium Isotope Compositions of Hydrothermal Barite from the Yonaguni IV: Insight into Fluid/Sediment Interaction and Barite Crystallization Condition. *J. Ocean Univ. China* 19, 377–385. doi: 10.1007/s11802-020-4021-4
- Zhou, Y., Zhang, D., Zhang, R., Liu, Z., Tao, C., Lu, B., et al. (2018). Characterization of vent fauna at three hydrothermal vent fields on the Southwest Indian Ridge: Implications for biogeography and interannual dynamics on ultraslow-spreading ridges. *Deep-Sea Res. Part I* 137, 1–12.

Conflict of Interest: The authors declare that the research was conducted in the absence of any commercial or financial relationships that could be construed as a potential conflict of interest.

Publisher's Note: All claims expressed in this article are solely those of the authors and do not necessarily represent those of their affiliated organizations, or those of the publisher, the editors and the reviewers. Any product that may be evaluated in this article, or claim that may be made by its manufacturer, is not guaranteed or endorsed by the publisher.

Copyright © 2022 Lim, Kim, Kim, Kim, Kim, Zhang, Kwack and Xu. This is an open-access article distributed under the terms of the Creative Commons Attribution License (CC BY). The use, distribution or reproduction in other forums is permitted, provided the original author(s) and the copyright owner(s) are credited and that the original publication in this journal is cited, in accordance with accepted academic practice. No use, distribution or reproduction is permitted which does not comply with these terms.